

UNIVERSITEIT ANTWERPEN

Faculty of Science

Department of Physics

**Vortex Structure in Mesoscopic
Thin-Film Superconductors:
Formation of Vortex Shells**

Thesis submitted for obtaining the degree of Advanced Master in
Nanophysics at the University of Antwerp by

Ben Xu

Promotor: Prof. dr. F. M. Peeters

Co-promotor: Dr. V. R. Misko

Academic year 2005-2006

Antwerpen

Contents

1	Introduction	1
1.1	Introduction to Superconductivity	1
1.1.1	General properties of superconductors	1
1.1.2	Theory of superconductivity	2
1.1.3	Fluxoid quantization	8
1.1.4	Vortex state	9
1.2	Vortex matter in mesoscopic superconductors	10
1.3	Vortex states in mesoscopic disks	11
1.3.1	Multivortex vs giant vortex	11
1.3.2	Vortex molecules and vortex lattice	15
2	Vortex shells in mesoscopic superconducting disks	17
2.1	Shells of vortices in mesoscopic disks	18
2.2	Shells in other systems	21
2.2.1	Shells in charged particles system	21
2.2.2	Shells of vortices in superfluid	22
2.3	Experimental observation of vortex shells	24
3	Theoretical approach	29

3.1	The Ginzburg-Landau equations for mesoscopic superconductor	
	29	
3.2	The London approximation	30
3.3	Molecular-dynamics simulation	32
3.3.1	General introduction to the molecular-dynamics method	32
3.3.2	Langevin molecular dynamics	34
3.4	Numerical procedure	35
4	Vortex configurations in mesoscopic SC disks	37
4.1	Formation of vortex shells	37
4.1.1	Vortex configurations for different vorticity numbers	37
4.2	The ground state of the vortex system	41
4.2.1	The possible configurations for a given vorticity L	41
4.2.2	The ground and metastable states	43
4.3	H - R phase diagram	46
4.3.1	Energy study of different vortex states	46
4.3.2	Phase diagram	48
4.3.3	Compare with the GL simulation	51
5	Conclusion	53
	References	55

1

Introduction

1.1 INTRODUCTION TO SUPERCONDUCTIVITY

1.1.1 General properties of superconductors

In 1911 H. Kamerlingh Onnes, observed that the resistance of mercury dropped sharply to zero at a temperature of 4.2K, just three years after he firstly liquefied helium. The same properties were later detected in some other metals. This new phenomenon was termed “superconductivity” and the corresponding metals were called “superconductors”. Perfect conductivity is the first traditional hallmark of superconductivity. The temperature at which the resistance disappears is called the *critical temperature*, T_c , it is different in different superconductors. For pure metals, the highest T_c is found for niobium: $T_c = 9.25K$; the lowest has been found in tungsten: $T_c = 0.0154K$. Since that, lots of scientists were lured to the wave of finding high T_c superconducting materials: in 1986, K. Alex Müller and J. George Bednorz of IBM zurich found superconductivity in lanthanum-based cuprate perovskite material at about 35K [1]. And shortly after that, YBCO, raised the critical temperature to 92K. Until 2000, the highest transition temperature was detected for fluorinated Hg-1223 samples ($T_c = 138K$) [2].

The next hallmark to be discovered was perfect diamagnetism, found in 1933 by Meissner and Ochsenfeld [3], if a metal is placed in a magnetic field smaller than a certain value H_c , then upon transition into the superconducting state the field is expelled from its interior, i.e., the true field $\mathbf{B} = 0$ in the superconductor (recall that the magnetic induction \mathbf{B} is the average micro-

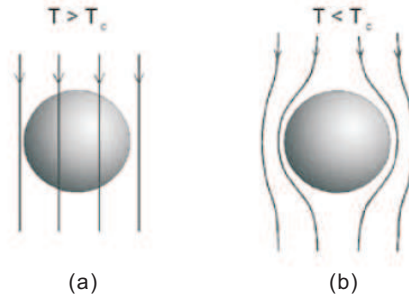


Fig. 1.1 Meissner effect in a superconducting sphere cooled under the critical temperature in a constant applied magnetic field. Below the transition temperature, the magnetic field lines are ejected from the sphere (Ref. [3])

scopic field). This is the so-called Meissner effect. This is illustrated in Fig. 1.1(a) for a normal metal; and (b) for a superconductor.

The existence of a reversible Meissner effect implies that superconductivity will be destroyed not only by increasing the temperature, but also by a *critical magnetic field* H_c which is related thermodynamically to the free-energy difference between normal and superconducting states in zero field, the so-called condensation energy of the superconducting state. The critical field in which superconductivity is destroyed decreases with increasing temperature. It has been established empirically that the dependence $H_c(T)$ is described well by the formula

$$H_c(T) = H_c(0) \left[1 - \left(\frac{T}{T_c} \right)^2 \right]. \quad (1.1)$$

Also superconductivity is destroyed by a strong electric current. If the superconductor is not too thin, the critical current j_c , at which resistance appears satisfies Silsbee's rule (Silsbee 1916): the magnetic field produced by the critical current at the surface of a superconductor must be equal to H_c .

1.1.2 Theory of superconductivity

A theoretical understanding of the phenomena associated with superconductivity has been reached in several ways. Many important results can be described by phenomenological equations: the London equations (1935) and the Ginzburg-Landau equations (1950). A successful microscopic theory of superconductivity was given by Bardeen, Cooper, and Schrieffer (BCS) (1950).

1.1.2.1 London theory The first attempt to develop the electrodynamics of superconductors was undertaken by the brothers F. London and H. London. The purpose of this theory was to express in mathematical form the basic

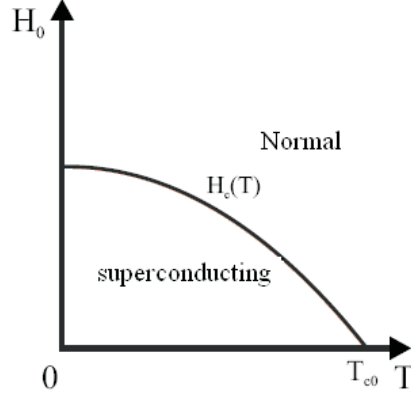


Fig. 1.2 Temperature dependence of critical field.

experimental facts: the absence of resistance and the Meissner effect, without consideration of the microscopic factors responsible for superconductivity.

If an electron does not undergo scattering, it is accelerated by an external field and, hence,

$$m^* \frac{d\vec{v}_s}{dt} = -e^* \vec{E}, \quad (1.2)$$

where m^* is the mass of the charge carriers, e^* is the charge of the carriers, \vec{v}_s is the supercurrent velocity, and \vec{E} is the applied electric field. Noticing, the full derivative signifies the variation of the quantity in a given volume element moving together with the liquid. It is connected with the partial derivative, which describes the variation at a given point of space by the relation

$$\frac{d}{dt} = \frac{\partial}{\partial t} + \mathbf{v} \cdot \nabla. \quad (1.3)$$

Since the real current velocities \mathbf{v} in a metal are small compared to the Fermi velocity, we can replace the total derivative by a partial derivative. And introducing $\mathbf{j} = n_s e^* \mathbf{v}_s$, where n_s is the superconducting carrier density and e^* is the charge of the carriers is the charge, we can rewrite formula (1.2) for the current density.

$$\frac{\partial \vec{j}_s}{\partial t} = \frac{n_s e^{*2}}{m^*} \vec{E}. \quad (1.4)$$

According to the general equation of electrodynamics:

$$\vec{\nabla} \times \vec{E} = \frac{1}{c} \frac{\partial \vec{H}}{\partial t}, \quad (1.5)$$

one obtains the following relation:

$$\frac{\partial}{\partial t} \left[\vec{\nabla} \times \vec{j}_s + \frac{n_s e^2}{m^* c} \vec{\mathbf{H}} \right] = 0. \quad (1.6)$$

This result is true for any perfect conductor, which means that the magnetic field $\vec{\mathbf{H}}$ and the temporally current \vec{j}_s is conserved. Hence, a magnetic field that penetrated the sample in the normal state would be locked into the interior of the crystal as it passed into the superconducting phase. This does not happen in reality, so then quantity in the square brackets is not simply conserved but is always equal to zero, which brings out:

$$\vec{\nabla} \times \vec{j}_s = -\frac{n_s e^2}{m^* c} \vec{\mathbf{H}}. \quad (1.7)$$

This equation states that dissipationless supercurrents flow at the surface of the crystal to completely shield the sample interior from the external magnetic field. Moreover, the above relation also predicts that any magnetic flux initially passing through the crystal will be completely expelled upon entering into the superconducting state.

The combination of the Eq.(1.7) with Maxwell equation for the magnetic field $\vec{\nabla} \times \vec{\mathbf{H}} = 4\pi \vec{j}_s / c$ leads to

$$\vec{\nabla}^2 \vec{\mathbf{H}} = \frac{1}{\lambda_L^2} \vec{\mathbf{H}}, \quad (1.8)$$

with

$$\lambda_L = \sqrt{\frac{m^* c^2}{4\pi n_s e^2}}. \quad (1.9)$$

The solution to this second order partial differential equation for a slab is simply a decaying exponential of the form $H = H' \exp(-x/\lambda_L)$. Thus one defines the first characteristic length scale of a superconductor, λ_L , the London penetration depth, which is the direct analog of the skin depth in a metal. It is simply the characteristic length that an external magnetic field can penetrate into the bulk of a superconducting crystal before decaying away. For atomic superconductors like Pb, Hg and Sn, the penetration depth is on the order of nanometers.

1.1.2.2 Ginzburg-Landau theory The Ginzburg-Landau theory extends Landau's theory of second-order phase transitions [4] to a spatially varying complex order parameter $\psi(\vec{r})$ ($|\psi(\vec{r})|^2 = n_s/2$ is a complex order parameter which is nonzero at $T < T_c$ and vanishes at $T \geq T_c$ through a second order phase transition). The resulting gradient term is made gauge-invariant by combining it with the vector potential $\vec{A}(\vec{r})$ where $\vec{\nabla} \times \vec{A}(\vec{r}) = \vec{\mathbf{H}}(\vec{r})$ is the local magnetic field.

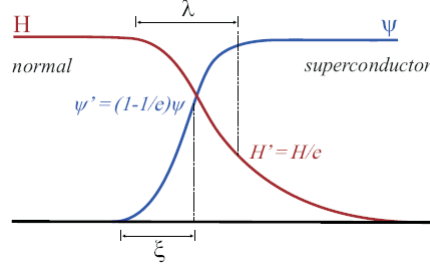


Fig. 1.3 The spatial distribution of the order parameter Ψ and the magnetic field h at the superconducting/normal surface boundary (after Ref. [5])

The two Ginzburg-Landau equations are obtained by minimization of the GL free energy functional $\mathcal{F}\{\psi, \vec{A}\}$ with respect to ψ and \vec{A} , i.e. from $\delta\mathcal{F}/\delta\psi = 0$ and $\delta\mathcal{F}/\delta\vec{A} = 0$:

$$\mathcal{F}\{\psi, \vec{A}\} = \frac{H_c^2}{4\pi} \int [-|\psi|^2 + \frac{1}{2}|\psi|^4 + \frac{1}{2}|(-i\nabla - \mathbf{A})\psi|^2 + \kappa^2(\vec{H} - \vec{H}_0)^2] dV, \quad (1.10)$$

where \vec{H}_0 denotes the applied magnetic field. Eq. (1.10) is given in dimensionless form, where all distances are measured in units of the coherence length ξ , the vector potential \vec{A} in $c\hbar/2e\xi$, the magnetic field \vec{H} in $H_{c2} = c\hbar/2e\xi^2 = \kappa\sqrt{2}H_c$, and the order parameter ψ in $\psi_0 = \sqrt{-\alpha/\beta}$, such that $|\psi| = 1$ in the Meissner state and $|\psi| = 0$ in the normal conducting state, with α, β being the GL coefficients.

The Ginzburg-Landau theory introduces two important characteristic length scales: the coherence length $\xi(T)$ and the penetration depth $\lambda(T)$. The coherence length $\xi(T)$ indicates the typical length scale over which the size of the order parameter can vary (Fig.1.3). The typical length scale over which the magnetic field \vec{H} varies is the penetration depth $\lambda(T)$. The first and second Ginzburg-Landau equations are, respectively:

$$\alpha\psi + \beta|\psi|^2\psi + \frac{1}{2m^*}(-i\hbar\nabla - \frac{2e}{c}\mathbf{A})^2\psi = 0, \quad (1.11)$$

$$\vec{j}_s = -\frac{i\hbar e}{m^*}(\psi^*\vec{\nabla}\psi - \psi\vec{\nabla}\psi^*) - \frac{4e^2}{m^*c}|\psi|^2\vec{A}. \quad (1.12)$$

In this discussion, weak magnetic field is applied, and the sample dimensions are much larger than the magnetic penetration depth. In a first order approximation, the value of Cooper-pair density can be replaced by its equilibrium zero-field value

$$|\psi| = \psi_0 = \sqrt{-\frac{\alpha}{\beta}}. \quad (1.13)$$

And now taking curl of both sides of the second GL equation, it becomes

$$\text{curl} \vec{j}_s = -\frac{4e^2}{m^*c} |\psi|^2 \text{curl} \vec{A} \quad (1.14)$$

Using Eq. (1.7) and Maxwell equation, and taking into account that $\alpha < 0$, this can be rewritten as

$$\vec{H} + \frac{m^*c^2\beta}{16\pi e^2|\alpha|} \text{curl} \text{curl} \vec{H} = 0, \quad (1.15)$$

which, upon comparing to the expression in Eq. (1.8), gives

$$\lambda(T) = \sqrt{\frac{m^*c^2}{16\pi e^2|\psi|^2}} = \sqrt{\frac{m^*c^2}{8\pi e^2n_s}} = \sqrt{\frac{m^*c^2\beta}{16\pi e^2|\alpha|}} \quad (1.16)$$

where the density of superconducting electrons $n_s = 2|\psi|^2 = 2|\alpha|/\beta$ and the mass of a Cooper-pair is twice the electron mass $m: m^* = 2m$.

Let us now consider a second example where ψ varies only in the z-direction, but the applied magnetic field is zero. In this case the first GL equation (1.11) becomes

$$-\frac{\hbar^2}{2m^*} \frac{d^2}{dz^2} \Psi + \alpha \Psi + \beta \Psi^3 = 0, \quad (1.17)$$

Assuming Ψ is real, we can introduce a dimensionless order parameter

$$\Psi = f \Psi_0, \quad (1.18)$$

where ψ_0 , corresponding to the state with lowest free energy when $\alpha < 0$, and is given by Eq. (1.13). Thus Eq. (1.17) becomes

$$-\frac{\hbar^2}{2m^*|\alpha|} \frac{d^2 f}{dz^2} - f + f^3 = 0. \quad (1.19)$$

A natural length scale for spatial variations of the order parameter is therefore

$$\xi(T) = \sqrt{\frac{\hbar^2}{2m^*|\alpha|}}, \quad (1.20)$$

which is known as the GL coherence length. Note that both the GL coherence length and the GL penetration depth are temperature dependent quantities, since α depends on the temperature as $\alpha \propto (T - T_{c0})$. It is therefore clear that both λ and ξ are proportional to $(1 - T/T_{c0})^{-1/2}$. One should notice that these characteristic lengths diverge at the critical temperature T_{c0} . The exact temperature dependence of ξ and λ depends on the purity of the material, defined by the elastic mean free path l_{el} [5, 6].

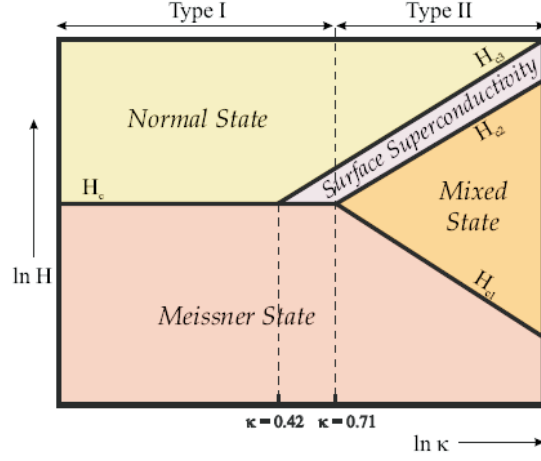


Fig. 1.4 The dependence of the characteristics of bulk superconductors on the value of the Ginzburg-Landau parameter κ . H_c and $H_{ci}|_{i=1-3}$ are explained in the text and denote the critical fields determining regions with different behavior of the superconductor (Ref.[7]).

1.1.2.3 Type-I and type-II superconductors The value of the Ginzburg-Landau parameter $\kappa = \lambda(T)/\xi(T)$ determines the behavior of a bulk superconductor in an applied magnetic field (H_0). Depending on κ being smaller or larger than $1/\sqrt{2} \simeq 0.71$, a distinction can be made between type-I and type-II superconductors:

$$\kappa < 1/\sqrt{2} \rightarrow \text{type - I superconductors,}$$

$$\kappa > 1/\sqrt{2} \rightarrow \text{type - II superconductors.}$$

All superconducting chemical elements except niobium are type-I superconductors. Besides niobium, all superconducting alloys, chemical compounds and the high- T_c superconductors belong to the second group. One should note that this rigid distinction holds only for bulk superconductors. The dependence of the superconducting characteristics on the value of κ is illustrated in Fig. 1.4. In mesoscopic samples, the behavior of the superconductor depends not only on κ but also on the geometrical parameters as well.

Bulk samples with $\kappa < 0.42$ are pure type-I superconductors. For fields below the thermodynamical critical field H_c the superconductor is in the Meissner state and all flux is expelled from the sample. At the critical field the magnetic field penetrates the sample, superconductivity is destroyed and the sample becomes normal. For $0.42 < \kappa < 1/\sqrt{2} \simeq 0.71$ we still consider the superconductor to be of type-I, although the Meissner state does not change immediately into the normal state with increasing field. At the field H_c flux

can penetrate the inner part of the sample, while near the surface of the sample, a layer remains superconducting (so-called surface superconductivity). For fields higher than the surface critical field H_{c3} the whole sample is in the normal state.

On the other hand, a type II superconductor ($\kappa > 0.71$) has a remarkably different behavior, as described below.

The Meissner effect in type-II superconductors is complete only in very weak fields, $H_0 < H_{c1}$. The lower critical field H_{c1} is much less than the thermodynamic critical field H_C .

At $H_0 > H_{c1}$ magnetic field lines penetrate the superconductor. Nevertheless, even in the equilibrium state the penetration is not complete. The flux ϕ is smaller than in the normal state, meaning that persistent currents still exist. Actually, the magnetic flux appears to be quantized in units of the flux quantum $\phi_0 = hc/2e$, and penetrates the superconductor in the form of vortices. In 1957, Abrikosov found that these vortices construct a triangular lattice inside the superconductor. Such a situation holds at $H_{c1} < H_0 < H_{c2}$ where H_{c2} is the so-called upper critical field, much larger than H_c . Such a magnetic field range with partial field penetration in the superconductor has been discovered by Shubnikov (1937) and is called the Shubnikov phase. Another name for this region is the *Abrikosov vortex state*, or the mixed state.

At $H_0 > H_{c2}$ a macroscopic sample does not repel the flux, and $B \equiv H$. At the same time, at $H_{c2} < H_0 < H_{c3}$ a thin surface superconducting layer still exists (for bulk superconductors $H_{c3} = 1.69H_{c2}$). After H_{c3} field is exceeded, superconductivity is destroyed and the entire sample is in the normal state.

1.1.3 Fluxoid quantization

For the second Ginzburg-Landau equation Eq. (1.12), we introduce the magnitude $|\psi|$ and the phase ϕ of the order parameter, and rewrite the equation as:

$$\vec{j}_s = \frac{2e\hbar}{m}|\psi|^2\vec{\nabla}\phi - \frac{4e^2}{mc}|\psi|^2\vec{A}. \quad (1.21)$$

Let us now calculate the contour integral of the vector potential around a closed path C, i.e.

$$\oint_C \vec{A} \cdot \vec{l} = \int \text{curl} \vec{A} \cdot d\vec{S} = \int \vec{H} \cdot d\vec{S} = \Phi.$$

This integral obviously gives the magnetic flux through the contour C. Using Eq. (1.22), we obtain

$$\Phi = \oint \vec{A} \cdot \vec{l} = -\frac{mc}{4e^2} \int_C \frac{\vec{j}_s}{|\psi|^2} \cdot \vec{l} + \frac{c\hbar}{2e} \int_C \vec{\nabla}\phi \cdot \vec{l}. \quad (1.22)$$

The last integral does not necessarily vanish, because the only general requirement is that the modulus of the order parameter ψ is a single valued

function. i.e. the phase of ψ varies by $2\pi n$, where n is an integer, when we make a complete turn around C . Consequently, Eq. (1.23) predicts the fluxoid quantization

$$\Phi = \oint \vec{A} \cdot \vec{l} = -\frac{mc}{4e^2} \int_C \frac{\vec{j}_s}{|\psi|^2} \cdot \vec{l} + \frac{ch}{2e} \int_C \vec{\nabla} \phi \cdot \vec{l}. \quad (1.23)$$

If the path of integration is chosen to be a contour where $\vec{j}_s = 0$, or j_s is orthogonal to $d\vec{l}$, the relation becomes $\Phi = n\Phi_0$, showing that the flux trapped in a superconductor is quantized in flux quanta Φ_0 , given by:

$$\Phi_0 = ch/2e = 2.067 \times 10^{-7} \text{Gs cm}^2, \quad (1.24)$$

with $h = 2\pi\hbar$.

1.1.4 Vortex state

The penetration of vortices into type-II superconductors was predicted first by A. A. Abrikosov when he discovered a two-dimensional periodic solution of the Ginzburg-Landau (GL) equations[39]. Abrikosov correctly interpreted this solution as a periodic arrangement of flux lines, the flux-line lattice. Each flux line (or fluxon, vortex line) carries one quantum of magnetic flux Φ_0 , see Eq. (1.24), which is caused by the supercurrents circulating around vortex. The magnetic field peaks at the vortex positions. The vortex core is a tube in which superconductivity is weakened; the position of the vortex is defined by the line at which the superconducting order parameter vanishes. For well separated or isolated vortices, the radius of the tube of magnetic flux equals the magnetic penetration depth λ , and the core radius is somewhat larger than the superconducting coherence length ξ , see Fig. 1.5(a). With increasing applied magnetic field, the spacing a_0 between the vortices decreases, consequently the average flux density \bar{B} increases, and one has $\bar{B} = 2\Phi_0/\sqrt{3}a_0^2$ for the triangular flux-line lattice, see Fig. 1.5(b). The flux tubes then overlap such that the periodic induction $B(x, y)$ is nearly constant, with only a small relative variation about its average \bar{B} . With further increase of \bar{B} also the vortex cores begin to overlap such that the amplitude of the order parameter decreases until it vanishes when \bar{B} reaches the upper critical field $B_{c2} = \mu_0 H_{c2} = \Phi_0/(2\pi\xi^2)^2$, where superconductivity disappears.

When the thickness of a superconducting film d is smaller than the London penetration depth ($d < \lambda$), some consequences for the vortex structure arises. In a perpendicular magnetic field, the distance over which the field can be screened is given by a thickness-dependent effective penetration depth λ_{eff} :

$$\lambda_{eff} = \frac{\lambda^2(T)}{d}. \quad (1.25)$$

Pearl was able to show [8] that this strongly affects the radial dependence of the circulating sheet current density and the magnetic field of a vortex; instead of

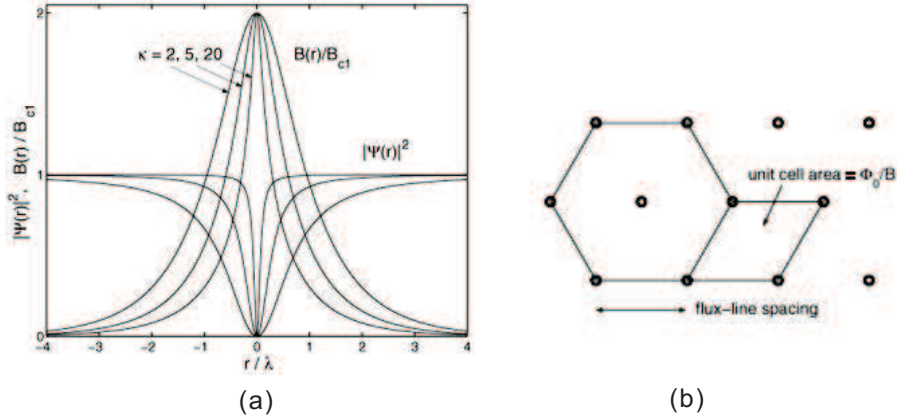


Fig. 1.5 (a) Magnetic field $B(r)$ and order parameter $|\psi|^2$ of an isolated flux line, calculated from Ginzburg-Landau theory for $\kappa = 2, 5$, and 20 ; (b) The triangular flux line lattice (from Ref. [9]).

the usual $\exp(-r/\lambda)$ dependence for large distances in bulk superconductors, the field decays only with $1/r^3$ in thin films. As a result, the interaction energy between vortices is changed to $U_{ij} \sim 1/r_{ij}$, similar to the Coulomb interaction between electric charges.

1.2 VORTEX MATTER IN MESOSCOPIC SUPERCONDUCTORS

Due to recent progress in microfabrication and measurement techniques, it is possible to study the properties of superconducting samples with sizes comparable to the penetration depth λ and the coherence length ξ . The behavior of such structures in an external magnetic field is strongly influenced by the boundary conditions and may lead to new superconducting states. In a circular system the superconducting state is characterized by a definite angular momentum that is similar to the Little-Parks oscillations [10] observed in a thin-film cylinder in the presence of an axial field.

In 1962, Little and Parks studied a thin-wire loop in an axial magnetic field. The $T_c - H$ phase diagram showed a periodic component. Each time a flux quantum $\phi_0 = hc/2e$ penetrates the system, $T_c(H)$ exhibits an oscillation. Berger and Rubinstein [11] studied nonuniform mesoscopic superconducting loops using the nonlinear Ginzburg-Landau (GL) theory. They assumed that the induced magnetic field can be neglected for samples with sufficiently small thickness. In the limit of thin loops, the transition between states with different angular momentum L (also called vorticity) occurs when the enclosed flux Φ equals $(L + 1/2)\phi_0$ [5]. The superconducting disk was studied by Schweigert et al [13, 14, 15, 17](see also [18]) by solving the two

GL equations self-consistently. Although the GL equations were derived to describe superconductivity near the critical point, this theory turns out to be valid over a much broader range of magnetic field and temperature [17][19]. They found that the finite thickness of the disk influences the magnetic field profile, i.e., the magnetic pressure, and this changes the size of the Meissner effect, which is different from the well-studied cylinder geometries [20]. The reverse problem, i.e., the antidot, was studied by Bezryadin et al. [21]. They obtained a phase diagram of a thin superconducting film with a circular hole in an axial magnetic field by solving numerically the nonlinear GL equations in the limit of a thin film.

The intermediate case of finite width loops was studied previously by Bardeen [22] within the London theory. He showed that in tubes of very small diameter and with wall thickness of the order of the penetration depth the flux through the tube is quantized in units of $v\phi_0$, where $v < 1$. Recently, square loops with attached leads were studied in [23]. It was found that the distribution of Cooper pairs is strongly inhomogeneous in the loop with enhancements near the corner of the square loop. Bruyndoncx et al. [24] investigated infinitely thin loops of finite width. In this case, the magnetic field induced by the supercurrents can be neglected and the total magnetic field equals the external applied magnetic field.

Not only samples' shape but also its symmetry influences the nucleation of superconductivity and can lead to new vortex states with antivortices. For instance, superconductivity in mesoscopic equilateral triangles, squares, etc., in the presence of a magnetic field nucleates by conserving the imposed symmetry (C_3, C_4) of the boundary conditions [25] and the applied vorticity. In an equilateral triangle, for example, in an applied magnetic field H generating two flux quanta, $2\Phi_0$, superconductivity appears as the C_3 -*symmetric* combination $3\Phi_0 - \Phi_0$ (denoted as "3-1") of three vortices and one antivortex in the center. A thermodynamically stable vortex-antivortex pattern has been revealed [26] in equilateral mesoscopic type I superconducting triangles, contrary to type II superconductors where similar patterns are unstable. The stable vortex-antivortex "molecular" appears due to the interplay between two factors: a repulsive vortex-antivortex interaction in type I superconductors and the vortex confinement in the mesoscopic triangle.

1.3 VORTEX STATES IN MESOSCOPIC DISKS

1.3.1 Multivortex vs giant vortex

When the dimensions of the disk are comparable to the coherence length ξ only few vortices can coexist in the system. In contrast to the usual triangular arrangement in bulk, complex and unique vortex structures are expected to occur due to the competition between surface superconductivity and vortex-vortex interaction.

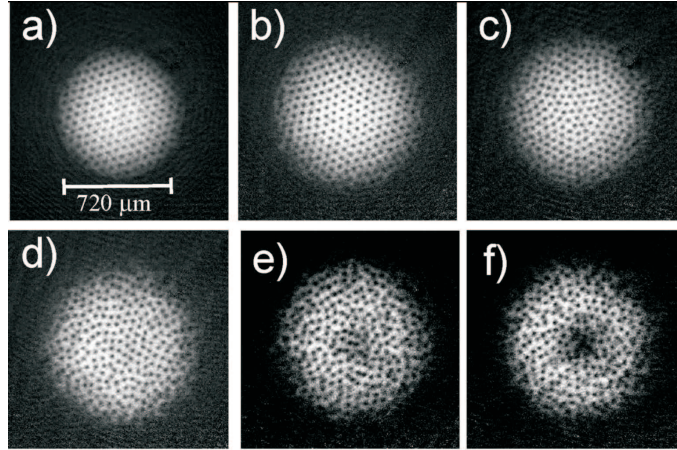


Fig. 1.6 Different stages of giant vortex formation process. (a) Starting point: BEC after evaporative spin-up. (b)-(f) Laser shone onto BEC for (b) 14s, (c) 15s, (d) 20s, (e) 22s, (f) 23s (from Ref. [12]).

Theoretical studies have shown that in mesoscopic disks surrounded by vacuum or an insulator medium two kinds of superconducting states can exist. First, there is a circular symmetric state with a fixed value of the angular momentum (or the giant vortex). This so called giant vortex can carry several vortex quanta. The observed magnetization jumps correspond to first-order phase transitions between the giant vortices with different angular momentum [13, 14]. Second, in disks with a sufficiently large radius multivortex structures can exist which are the analogue of the Abrikosov flux-line lattice in a bulk superconductor. These states can be represented as a mixture of giant vortex ones with different angular momentum. For multivortex states it is also possible to introduce an effective total angular momentum, which is nothing else than the number of vortices in the disk, i.e., the vorticity. With changing the magnetic field there is a second-order phase transition between the multivortex and the giant vortex state [15].

I. R. Coddington *et al.* [12] investigated the formation of the giant vortex. In their experiment the formation of the giant vortex comes about in a sequence of very distinct stages as shown in Fig. 1.6. For this expansion image sequence a rapidly rotating BEC is first formed by their evaporative spin-up technique. Then the atom-removal laser is applied with a fixed power of 8 fW for a variable amount of time, followed by a 10 ms in-trap evolution time and a 45ms expansion in the antitrapping configuration described above. Fig. 1.6(a) shows the result of only the evaporative spin-up. This particular condensate contains 180 vortices and has a Thomas-Fermi radius of $63.5\mu\text{m}$ when held in the trap. When the atom removal laser is applied for 14 s as in Fig. 1.6(b), the number of vortices is increased to 250 and the Thomas-Fermi

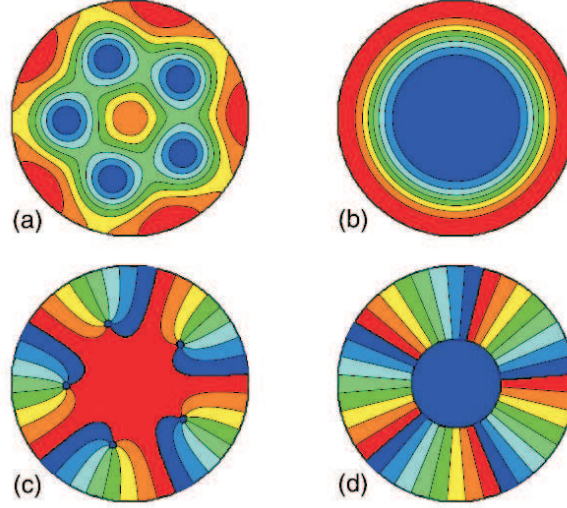


Fig. 1.7 The Cooper-pair density for the multivortex state (a) and the giant vortex state (b), and the phase of the order parameter for the multivortex state (c) and the giant vortex state (d) with vorticity $L = 5$ in a superconducting disk with radius $R/\xi = 6.0$. High (low) Cooper-pair density is given by red (blue) regions. Phases near 2π (0) are given by red (blue) (after Ref.[16])

radius to $71\mu m$. After atom removal times of 15 to 20s, the vortex lattice becomes disorderd [Fig. 1.6(c,d)], and the giant vortex core starts to develop in the center [Fig. 1.6(e,f)]. For The giant vortex state is characterized by the total angular momentum L through $\Psi = \psi(\rho)\exp(iL\phi)$, where ρ, ϕ are the cylindrical coordinates. An arbitrary superconducting state is generally a mixture of different angular harmonics. The effective angular momentum is defined as $L = \Delta\phi/2\pi$ does not depend on the loop radii ρ_l when it is in some range $\rho_l = (0.8 - 1)R$. And because the effective angular momentum is in fact nothing else then the number of vortices in the disk, so we can characterize unambiguously the different superconducting states by counting the effective angular momentum.

The dimensionless Gibbs free energies can be calculated by (of the different vortex configurations) $\mathcal{F} = V^{-1} \int [2(\vec{A} - \vec{A}_0) \cdot \vec{j}_{2D} - |\Psi|^4] d\vec{\tau}$, where integration is performed over the disk volume V , and \vec{A}_0 is the vector potential of the external uniform magnetic field. Having the free energies of different vortex configurations, Schweigert *et al.* [15] constructed an equilibrium vortex phase diagram which is shown in Fig. 1.8. For two disk radii $R = 4\xi$ and $R = 4.8\xi$, respectively. The solid curves separate the regions with a different number of vortices and the dashed curves show the boundaries between the multivortex and the giant vortex states. For $L = 1$ the single vortex state

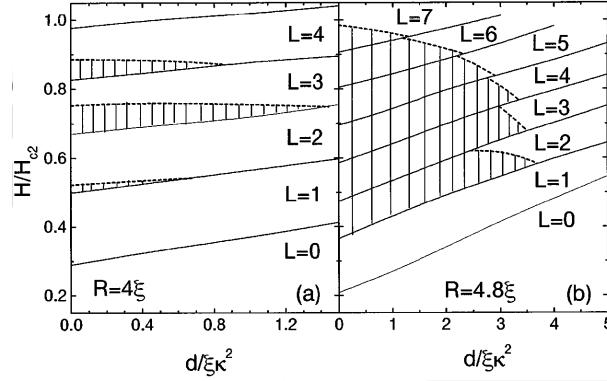


Fig. 1.8 The vortex phase diagram for two different disk radii $R=4\xi$ (a) and $R=4.8\xi$ (b). The shaded area corresponds to the multivortex state (after Ref.[15]).

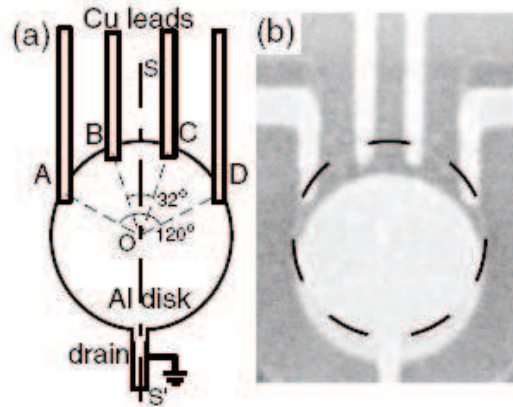


Fig. 1.9 Schematic view (a) and scanning electron micrograph (b) of the sample. The structure was fabricated using e -beam lithography followed by double-angle evaporation of Al and Cu. After the Al film was deposited, the surface of the Al film was slightly oxidized to provide the tunnel barrier. Most of the Al disk, indicated by the dashed circle, is covered with a Cu film (bright regions). We expect that the Cu film will not have any serious influence on the superconductivity of the Al disk because of the insulating AlO_x layer between them [40].

and the giant vortex state are identical. The shaded regions correspond to the multivortex states. The superconducting to normal transition occurs for $H/H_{c2} \approx 1.9$ which is outside the plotted region. Notice that the multivortex area in the phase diagram reduces in size with increasing disk thickness and it disappears in the limit of thick disks where only the giant vortex states survives. When increasing the radius of the disk, the energy difference between

different L states decreases and consequently it becomes possible to build a lower energy multivortex state out of a linear combination of giant vortex states. For a decreasing radius this is more difficult to do and there exists a critical radius below which no multivortex states have the lowest energy. To distinguish quantitatively the giant vortex states from the multivortex states for the same number of vortices we consider the value of the order parameter $|\Psi|^2$ in the center of the disk. They find that this parameter, which is zero for a giant vortex state, goes almost linearly to zero when the magnetic field approaches some critical value. Therefore, the magnetic field obtained by linearly interpolating $|\Psi(0,0)|^2$ to zero defines the transition from a multivortex state to a giant vortex state.

By studying the response of a mesoscopic superconducting disk to perpendicular magnetic fields, using the multiple-small-tunnel-junction method (see Fig. 1.9), in which transport properties of several small tunnel junctions attached to the disk are measured simultaneously[40], it became possible to experimentally distinguish the giant vortex states (GVSs) with a single core in the center and multivortex states (MVSs) with a spatial arrangement of singly quantized vortices.

1.3.2 Vortex molecules and vortex lattice

In a mesoscopic superconductor both the geometry and size of the specimen influence the vortex configurations, due to the interaction between vortices and the surface. Therefore, for small enough samples (with sizes comparable to ξ), the conventional hexagonal lattice predicted by Abrikosov no longer exists, and vortex configurations adjust to the sample geometry, yielding some kind of vortex molecule states [27]. For example, vortices arrange themselves in ring-like structures in disks with radii (R) a few times ξ . Nevertheless when an overlapping of vortices starts to take place, discrepancies between vortices and a picture based on particles arise, such as the formation of giant vortex states. Also, vortex-antivortex configurations may become possible for noncircular geometries.

In Ref. [27], they studied multivortex states in the range from few vortices - forming a ring-like structure - to many vortices, yielding a triangular lattice in the center of the disk and a ring-like structure close to the edges. Multivortex states were obtained for fields up to $H_0 \approx H_{c2}$, above which a giant vortex state appears. They found vortex configurations having ring-like distribution at low magnetic fields ($H_0 \ll 0.1H_{c2}$), as expected from symmetry considerations. However as the number of vortices increases, the vortex-vortex repulsion starts playing a larger role and they observed the appearance of an hexagonal lattice. The ringlike structure is replaced by an Abrikosov lattice in the center of the disk as soon as the field is close to $0.1H_{c2}$, when $L \sim 100$, but is preserved near the edges. For fields larger than $0.1H_{c2}$ this Abrikosov lattice becomes even more pronounced compared to the ring-like structure.

2

Vortex shells in mesoscopic superconducting disks

Vortices can be viewed as a specific type of quasiparticles interacting magnetically and through the encircling superconducting screening currents with each other. This makes confined vortex structures somewhat similar to other systems such as electrons in artificial atoms that exhibit complex self organized patterns for a small number of electrons [28, 29]. Similarly to Hund’s rule, it is expected that vortices will obey specific rules for shell filling and exhibit magic numbers. But, on the other hand, the present situation is expected to be complicated by the fact that vortices are not point-like objects. They can overlap and, contrary to electrons in artificial atoms, even join together creating a giant vortex state.

Until recently, only limiting cases were studied as concerns vortex distributions in mesoscopic disks: (1) disks with small radii in which at most a single ring of vortices can be present (see, for example, Refs. [13, 14, 30, 31]), and (2) infinitely extended superconducting films where the triangular Abrikosov vortex lattice is energetically favorable (see, for example Refs. [5, 6, 32]).

Several recent studies were devoted to the questions, how the vortices are distributed in disks over different shells, which vortex configuration is energetically most favorable, and how the transition between different vortex states occurs. Buzdin and Brison [33] studied vortex structures in superconducting disks using the image method, where vortices are considered to be point-like “particles”, i.e., the London approximation. Palacios calculated the vortex configurations in superconducting mesoscopic disks with radius equal to $R = 8.0\xi$, where two vortex shells can become stable [18]. He expanded the order parameter in normalized nodeless functions that diagonalize the kinetic-energy operator and limited the number of contributing terms to 3 or 4. The

demagnetization effects were included approximately by assuming the magnetic field everywhere to be equal to some effective field. Baelus, Cabral and Peeters [34] studied the vortex configurations in superconducting disks with $d \ll \lambda, \xi$ and $R = 6.0\xi$ and expanded the order parameter over all eigenfunctions with energy $\epsilon_i < \epsilon_*$, where the cutting energy ϵ_* was chosen such that increasing it does not influence the results. Geim *et al* [35] studied experimentally and theoretically the magnetization of different vortex configurations in superconducting disks. They found clear signatures of first- and second-order transitions within states of the same vorticity, which revealed the existence of different vortex configurations with the same vorticity. Schweigert and Peeters [36] studied the field-cooled vortex states in mesoscopic superconducting disks and cylinder.

2.1 SHELLS OF VORTICES IN MESOSCOPIC DISKS

In the work of Baelus, Cabral and Peeters [37] the distribution of vortices over different vortex shells in mesoscopic superconducting disks with sufficiently large sizes was investigated within the framework of the nonlinear Ginzburg-Landau theory. It was shown that there exists different vortex configurations for a certain total vorticity L . In these configurations the vortices are distributed differently over the vortex shells. In particular for a superconducting disk with radius $R = 6.0\xi$ and $d \ll \lambda$, the following vortex states were found:

(i) The $L = 0$ state or the Meissner state, and the $L = 1$ state where a single vortex is nucleated in the center of the disk. These states are denoted as 0-state and 1-state, respectively.

(ii) The multivortex state with vorticity L where all L vortices are separated and located on a single shell (ring) which occurs for vorticity $L = 2 - 8$. Notation: (n) -state with $n = L$. As an example the contour plots of the Cooper-pair density for the (4)-state and the (8)-state are shown in Figs. 2.1(a) and 2.1(b) Dark (light) regions correspond to high (low) Cooper-pair density.

(iii) The multivortex state with vorticity L with one vortex in the center while all the other vortices are positioned on a single shell around the center. They can be stable for $L = 6 - 11$. Notation: $(1, n)$ -state with $n = L - 1$.

(iv) The multivortex state with vorticity L with two vortices on an inner shell and the other vortices on an outer shell can nucleate for $L = 10 - 14$. Notation: $(2, n)$ -state with $n = L - 2$. When the two vortices in the center are combined into a giant vortex state with vorticity 2, one uses the notation $(2_g, n)$.

(v) The multivortex state with vorticity L with three vortices on an inner shell and the other vortices on an outer shell can be stable for $L = 12 - 14$. Notation: $(3, n)$ -state with $n = L - 3$.

(vi) The giant vortex state with vorticity L where all the L vortices are combined into one larger vortex in the center is possible for $L = 12 - 24$.

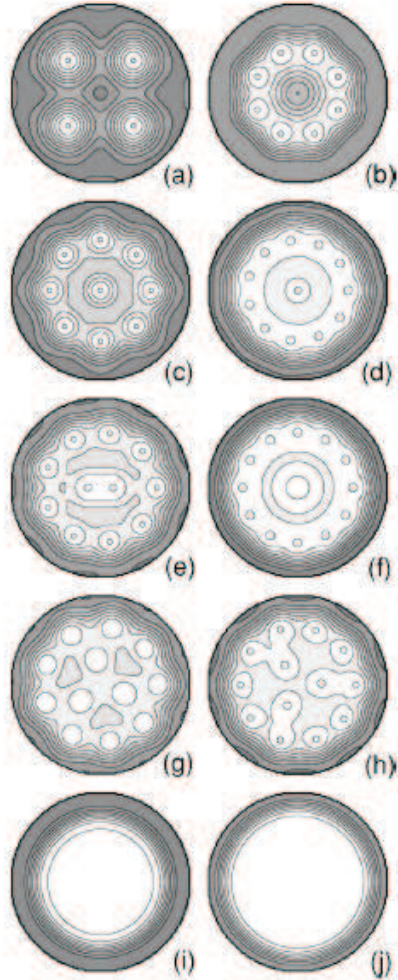


Fig. 2.1 Contour plots of the Cooper-pair density of the (4)-state at $H_0/H_{c2} = 0.3$ (a), the (8)-state at $H_0/H_{c2} = 0.7$ (b), the (1,8)-state at $H_0/H_{c2} = 0.7$ (c), the (1,11)-state at $H_0/H_{c2} = 0.8$ (d), the (2,9)-state at $H_0/H_{c2} = 0.8$ (e), the (2_g,12)-state at $H_0/H_{c2} = 0.93$ (f), the (3,9)-state at $H_0/H_{c2} = 0.82$ (g), the (3,10)-state at $H_0/H_{c2} = 0.88$ (h), the 15-state at $H_0/H_{c2} = 1.2$ (i), and the 24-state at $H_0/H_{c2} = 1.6$ (j). Dark (light) regions correspond to high (low) Cooper-pair density.

The difference in free energy between states with different vorticity is much larger than the free-energy difference between vortex states with the same vorticity but different vortex arrangements.

L	configurations				
number	stable	$metastable_1$	$metastable_2$	$metastable_3$	$metastable_4$
0	0
1	1
2	(2)
3	(3)
4	(4)
5	(5)
6	(6)
7	(1,6)	(7)
8	(1,7)	(8)
9	(1,8)
10	(2,8)	(1,9)
11	(2,9)	(1,10)
12	(2,10)	(3,9)	(1,11)	(12)	...
13	(2,11)	(3,10)	(1,12)	(13)	...
14	(2,12)	(2 _g ,12)	(1,13)	(3,11)	(14)

Table 2.1 Possible (meta) stable vortex configurations in a mesoscopic superconductor disk with $R = 6.0\xi$ and $d \ll \lambda, \xi$. (after Ref.[37])

In larger superconducting disks one expects more shells of vortices and also a larger varieties of possible stable vortex configurations for a fixed number of vorticity. As an example, disks with radius $R = 20\xi$ were considered in Ref. [37] for the case of 16 vortices. At the applied magnetic field $H_0 = 0.1H_{c2}$ they found three different vortex configurations with vorticity $L = 16$, i.e., the (5, 11)–state, the (4, 12)–state, and the (1, 5, 10)–state. The (1, 5, 10)–state has the lowest energy of these three states over their whole region of stability and the (4, 12)–state the highest one.

An overview of all the possible vortex configurations in a disk with radius $R = 6.0\xi$, their stability region, and the regions over which they are the ground state are given in Table 2.1. With increasing field the ground state changes as follows with increasing field: $0 \rightarrow 1 \rightarrow (2) \rightarrow (3) \rightarrow (4) \rightarrow (5) \rightarrow (6) \rightarrow (1, 6) \rightarrow (1, 7) \rightarrow (1, 8) \rightarrow (1, 9) \rightarrow (2, 9) \rightarrow 12 \rightarrow 13 \rightarrow 14 \rightarrow \dots \rightarrow 25 \rightarrow 26 \rightarrow \text{normal state}$.

2.2 SHELLS IN OTHER SYSTEMS

2.2.1 Shells in charged particles system

Shell structures in a system of charged particles have been investigated using a Monte Carlo study, carried out in a finite two-dimensional (2D) system of charged classical particles which are confined by a circular parabolic well. The ground-state configurations were found by static energy calculations. These structures have been analyzed using the Voronoi construction. A ‘‘Mendeleev’’ table for those classical 2D-like atoms was obtained. In Ref [29], a model system is used, with a finite number N of charged particles interacting through a repulsive Coulomb potential and moving in two dimensions. A confinement potential $V_c(r)$ keeps the system together.

The Hamiltonian for such a system is given by

$$H = \sum_{i=1}^N V_c(r_i) + \frac{q^2}{\epsilon} \sum_{j>i}^N \frac{1}{|\mathbf{r}_i - \mathbf{r}_j|}, \quad (2.1)$$

where ϵ is the dielectric constant of the medium, and $r_i \equiv |\mathbf{r}_i|$ is the distance of the i th electron from the center of the confinement potential. The first term in Eq. (2.1) represents the confinement potential, where parabolic confinement was considered.

$$V_c(r) = \frac{1}{2}m\omega_0^2 r^2. \quad (2.2)$$

The confinement frequency ω_0 defines the length and temperature scale in the system. Parabolic confinement is similar to the action of a uniform neutralizing background of charges. Consequently, changing the number of particles N will, on the average, not change the density of the system, which is determined by the strength of the confinement frequency ω_0 .

The standard Metropolis, or $M(RT)^2$, algorithm for Monte Carlo simulation is used with automatic choice of maximal displacements to ensure an acceptance probability of 0.5. The initial configurations are chosen as fragments of the perfect Wigner triangular lattice with some appropriate inter-electron spacing for a given number of electrons. The real ground-state configurations are then obtained during the Monte Carlo equilibration run at zero temperature. In order to check that there is a global minimum, the system is heated up and cooled down again to $T = 0$.

In the case of not too large systems their simulations indicate, that at low temperature the particles are localized on shells. In Table (2.2) the shell structures are summarized for different number of particles N . The electrons are arranged into shells with average inter-electron distance which depends both on the radius (shell number) for a particular structure and on the total number of electrons. The density increases with N but is lower for outer

Number of particles	configuration	Number of particles	configuration
1	(1)	8	(1,7)
2	(2)	9	(2,7)
3	(3)	10	(2,8)
4	(4)	11	(3,8)
5	(5)	12	(3,9)
6	(1,5)	13	(4,9)
7	(1,6)	14	(4,10)

Table 2.2 Ground-state configurations for the system of charge particles with parabolic-confinement potential. Shell structures (N_1, N_2, \dots) (after Ref. [29])

shells. For large systems it is found that the structure of the inner shells is very close to the one of a triangular lattice. Namely, almost all those electrons are sixfold coordinated, whereas outer shells consist of lower-coordinated electrons. Thus there is a competition between two types of ordering: ordering into a triangular-lattice structure (Wigner lattice) and ordering into a shell structure. The triangular-lattice structure is the ordered configuration for a 2D system of point particles while the shell structure is imposed by the circular symmetry of the confinement potential. For large systems the inner electrons have a quasi-triangular-lattice structure, the outer electrons are a bend triangular lattice with equal number of electrons on the last few shells.

2.2.2 Shells of vortices in superfluid

In the case of a rotating superfluid, studied in Ref. [38], it has been shown that the two-dimensional vortex patterns that occur in a rotating cylinder of superfluid ${}^4\text{He}$ were systematically ordered for numbers of vortice $N = 1, 2, \dots, 30, 37, 50$ using a prescription for their free energy that was independent of angular velocity and was based upon the justified omission of images.

The free energy per unit length of a system of N rectilinear vortices in a rotating cylindrical vessel is given by

$$f = - \sum_{j>i=1}^N \ln(r_i^2 + r_j^2 - 2r_i r_j \cos\theta_{ij})$$

$$+ \frac{1}{2} \sum_{i,j=1}^N \ln(1 + r_i^2 r_j^2 - 2r_i r_j \cos\theta_{ij})$$

$$-\omega \sum_{i=1}^N (1 - r_i^2) + N \ln(R/a). \quad (2.3)$$

In reduced units, $f = (r\pi/\rho\kappa^2)F$ and $\omega = (2\pi R^2/\kappa)\Omega$. Here ρ is the density of the superfluid, R is the radius of the bucket, a is the vortex core radius, r_i is the radial distance to the i th vortex from the axis of the cylinder in units of R (so that in these units the radius of the bucket is unity), and $\theta_{ij} = \theta_i - \theta_j$ is the angle between r_i and r_j . This function f must be minimized for all N and r_i to find the stable pattern for a given ω . This procedure can be carried out analytically for only small numbers of vortices, perhaps $N < 9$, corresponding to the equilibrium states for small values of ω .

L	configurations			
number	stable	<i>metastable</i> ₁	<i>metastable</i> ₂	<i>metastable</i> ₃
0	0
1	1
2	(2)
3	(3)
4	(4)
5	(5)	(1, 4)
6	(1, 5)	(6)
7	(1, 6)	(7)
8	(1, 7)
9	(1, 8)	(2, 4, 3)	(2, 3, 4)	(3, 6)
10	(2, 4, 4)	(2, 2, 4, 2)	(1, 9)	...
11	(3, 8)	(2, 9)
12	(3, 3, 6)	(3, 6, 3)	(4, 8)	...
13	(4, 9)	(3, 10)
14	(4, 10)	(5, 9)

Table 2.3 Possible (meta)stable vortex configurations for N quantized vortices in an unbounded, rotating fluid. The metastable represent a few of the stationary patterns that are known to be nearly stable, as opposed to stable(after Ref. [38]).

Numerically, a stable pattern of any number N can be found by the following iterative scheme. Begin with an arbitrary pattern of vortices and assign

to each vortex a vector equal to the negative gradient of the free energy with respect to its coordinates: $\vec{u}_i = -\frac{1}{2}\vec{\nabla}_i f$. Move each vortex a step proportional to \vec{u}_i , then calculate the new values of \vec{u}_i and repeat. Each iteration produces a pattern of lower free energy if the constant multiplying each \vec{u}_i is sufficiently small. Eventually, the positions converge (as all \vec{u}_i approach zero) to a pattern which minimizes f , at least with respect to small displacements of the vortex positions.

Table 2.3 gives possible configurations which exist in the rotating superfluid system for $L < 15$. The stable arrays are the result of two competing effects. First, the vortices effectively repel each other and try to stay apart and, second, the pattern would like to be round and compact. The first force represents a pair-wise repulsive interaction which drops off as $1/r$ while the second is a harmonic-like attraction to the axis of the bucket with strength proportional to ω . As N increases, the pattern with lowest free energy changes from 1 in the center to 2, 3, 4, 5, and then back to 1 ($N = 16$), 2 ($N = 10$), 3, 4, 5, and again 1 ($N = 17$). This cycle then repeats. Having 1 vortex in the center of the lowest energy pattern is presumably a property of vortex numbers close to those with “triangular” ring numbers, $N = 1 + 6(1 + 2 + 3 \dots) = 1, 7, 19, 37, \text{etc.}$

2.3 EXPERIMENTAL OBSERVATION OF VORTEX SHELLS

Recently, the first direct observation of rings of vortices in mesoscopic Nb disks was performed by Grigorieva *et al* [42], using Bitter decoration technique. They studied the formation of concentric shells of vortices for a broad range of vorticities L . From images obtained for disks of different sizes in a range of magnetic fields, they traced the evolution of vortex states and identified stable and metastable configurations of interacting vortices. Furthermore, the analysis of shell filling with increasing L allowed them to identify magic number configurations corresponding to the appearance of consecutive new shells.

They studied the behavior of vortices in two ways.

(i) They trace the exact evolution of vortex states as L increased with increasing flux. States with different L are realized over overlapping intervals of Φ and their evolution follows a well-defined pattern. The first 5 vortices are added one by one to form the first shell, the second shell appears at $L = 6$ [state (1,5)] in the form of one vortex in the center, and this configuration remains stable until $L = 9$ is reached, i.e., the next 3 vortices are added to the outer shell. The inner shell begins to grow at $L = 9$, with the next two states having 2 vortices in the center [(2,7) and (2,8)], the following two states having 3 vortices in the center [(3,7) and (3,8)], and so on. It is clear that, despite the presence of pinning, vortices generally form circular configurations

expected for a disk geometry; i.e., the effect of confinement dominates over pinning.

The experimentally observed process of shell filling for all L up to 40 is summarized in Fig. 2.2(b). For $L = 12$ to 16, vortices are added intermittently to either the outer or the inner shell. At $L = 17$, a third shell appears with one vortex formed in the center. The next 3 vortices are added to the outermost shell, after which all three shells grow intermittently until $L = 32$. And the fourth shell appears at $L = 33$ in the form of one vortex in the center. At larger $L > 40$, vortices in the center no longer “feel” the presence of the boundary, and pinning is only opposed by vortex-vortex interactions.

(ii) For $L \leq 4$ only one vortex configuration was found for each L . For larger L , unexpected multiplicity of states were observed for the same L and Φ , for example, two vortex configurations were found for $L = 9$ and $L = 10$, which are demonstrated by histogram in Fig. 2.3. The explanation is that not only stable states of L interacting vortices of this were observed but also their metastable configurations. The results of such analysis are summarized in Table 2.4. Most configurations found experimentally agree with earlier numerical simulations [33, 37, 41]. However, some theoretically predicted configurations were not found in a few cases, such as the state (1,8) for $L = 9$. From the Table 2.4, one can see that the observed vortex configurations are in better agreement with those predicted for a finite system of charged particles and vortices in liquid helium. We will further discuss this issue in Chapter 4, where the vortex configurations are calculated which agree with the experiments from Ref. [42].

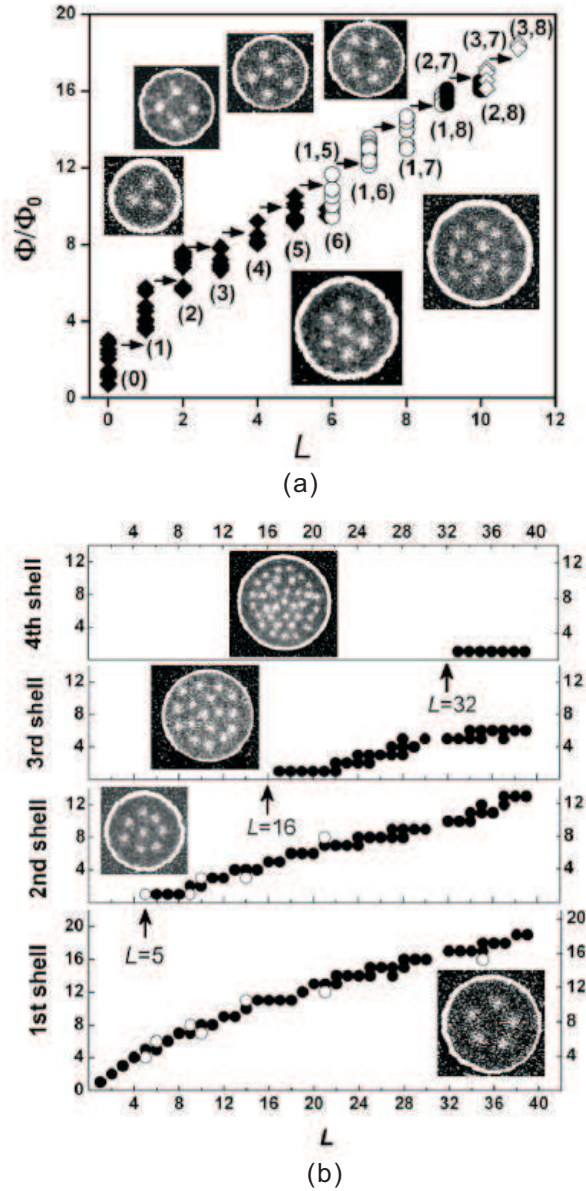


Fig. 2.2 (a) Evolution of vortex states with increasing Φ (arrows are guides to the eye). Different symbols correspond to different shell configuration: \blacklozenge , states (L) ; \circ , states $(1, L - 1)$; \bullet , states $(2, L - 2)$; \diamond , states $(3, L - 3)$. SEM images of some of the states are shown as insets: left to right states (3), (4), (1, 5), (6), (1, 6), and (3, 8). (b) Number of vortices populating different shells as a function of L . Two or more different states were found for some vorticities, e.g., (1, 7, 14) and (2, 7, 13) for $L = 22$. The first magic number, $L = 5$, corresponds to the stable state (5) rather than the metastable state (1, 4). Insets: SEM images of vortex states with different numbers of shells: 1-shell state (5) [$L = 5$]; 2- shell state (1, 7) [$L = 8$]; 3- shell state (1, 5, 11) [$L = 17$]; 4- shell state (1, 5, 11, 18) [$L = 35$] (after Ref. [42]).

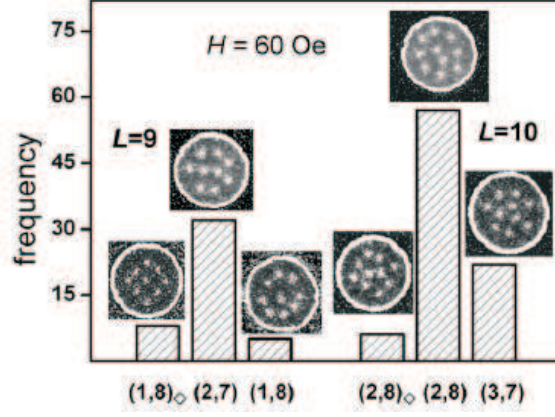


Fig. 2.3 Histogram of different vortex states observed in the same experiment ($H = 60 \text{ Oe}$) on disks with $d = 3 \mu\text{m}$. SEM images of the corresponding states are shown as insets. (Ref. [42])

L	S_{exp}	S_{theory}	MS_{exp}	MS_{theory}
1	(1)	(1) ^a	(1) ^b	(1) ^c
2	(2)	(2) ^a	(2) ^b	(2) ^c
3	(3)	(3) ^a	(3) ^b	(3) ^c
4	(4)	(4) ^a	(4) ^b	(4) ^c
5	(5)	(5) ^a	(5) ^b	(5) ^c
6	(1,5)	(6) ^a	(1,5) ^b	(1,5) ^c
7	(1,6)	(1,6) ^a	(1,6) ^b	(1,6) ^c
8	(1,7)	(1,7) ^a	(1,7) ^b	(1,7) ^c
9	(2,7)	(1,8) ^a	(1,8) ^b	(2,7) ^c
10	(2,8)	(1,9) ^a	(2,8) ^b	(2,8) ^c
11	(3,8)	(2,9) ^a	(3,8) ^b	(3,8) ^c

^a Results of Ref. [37] for superconducting vortices

^b Vortices in He, Ref. [38]

^c Charged particles, Ref. [29]

Table 2.4 Comparison of experimentally observed stable S_{exp} and MS_{exp} states for $1 \leq L \leq 11$ with those found numerically. Only stable (ground) states were calculated in Ref[12]

3

Theoretical approach

3.1 THE GINZBURG-LANDAU EQUATIONS FOR MESOSCOPIC SUPERCONDUCTOR

In the theoretical work of Baelus, Cabral and Peeters [37], they considered thin superconducting disks immersed in an insulating medium in the presence of a perpendicular uniform magnetic field H_0 . As for thin disks ($d \ll \xi, \lambda$) it is allowed to average the Ginzburg-Landau (GL) equations over the disk thickness. Using dimensionless variables and the London gauge $\text{div } \vec{A} = 0$ for the vector potential \vec{A} , one can write the system of GL equations in the following form:

$$(-i\vec{\nabla}_{2D} - \vec{A})^2\Psi = \Psi(1 - |\Psi|^2), \quad (3.1)$$

$$-\Delta_{3D}\vec{A} = \frac{d}{\kappa^2}\delta(z)\vec{j}_{2D}, \quad (3.2)$$

where

$$\vec{j}_{2D} = \frac{1}{2i}(\Psi^*\vec{\nabla}_{2D}\Psi - \Psi\vec{\nabla}_{2D}\Psi^*) - |\Psi|^2\vec{A}, \quad (3.3)$$

is the density of superconducting current. The superconducting wave function satisfies the boundary conditions $(-i\vec{\nabla}_{2D} - \vec{A})\Psi|_n = 0$ normal to the sample surface and $\vec{A} = \frac{1}{2}H_0\rho\vec{e}_\phi$ far away from the superconductor. The superconductor is placed in the (x,y) plane, the external magnetic field is directed along the z axis, and the indices 2D, 3D refer to two- and three-dimensional operators, respectively.

To solve the system of Eqs. (3.1) and (3.2), one can use the approach of Ref. [15] for circular disks. They apply a finite difference representation for the

order parameter and the vector potential on a uniform Cartesian space grid (x,y) , with typically 128×128 grid points for the area of the superconductor, and use the link variable approach, and the iteration procedure based on the Gauss-Seidel technique to find Ψ . The vector potential is obtained with the fast Fourier-transform technique where we set $\vec{A}_{|x|=R_s,|y|=R_s} = H_0(x, -y)/2$ at the boundary of a box with a larger space grid of size typically four times the superconductor area.

For circular configurations such as disks the giant vortex state is characterized by the total angular momentum L through $\Psi = \psi(\rho)\exp(iL\phi)$, where ρ and ϕ are the cylindrical coordinates. L is the winding number and gives the vorticity of the system. Due to the nonlinearity of the GL equations an arbitrary superconducting state is generally a mixture of different angular harmonics L even in axially symmetric systems. Nevertheless, they can introduce an analog to the total angular momentum L which is still a good quantum number and which is in fact nothing else but the number of vortices in the system.

To find different vortex configurations, which include the metastable states, one has to search for the steady-state solutions of Eqs. (3.1) and (3.2) starting from different randomly generated initial conditions. Then they increase/decrease slowly the magnetic field and recalculate each time the exact vortex structure. This is done for each vortex configuration in a magnetic-field range where the number of vortices stays the same. By comparing the dimensionless Gibbs free energies of the different vortex configurations

$$\mathcal{G} = V^{-1} \int_V [2(\vec{A} - \vec{A}_0) \cdot \vec{j}_{2D} - |\Psi|^4] d\vec{r}, \quad (3.4)$$

where integration is performed over the sample volume V and \vec{A}_0 is the vector potential of the uniform magnetic field, the ground state was found.

3.2 THE LONDON APPROXIMATION

For the London approximation, we follow the approach outlined in Refs. [33, 37]. In this limit the order parameter is considered uniform throughout the disk, except for small regions with areas of the order of ξ^2 , where it drops to zero. This approximation is justified when $\kappa \gg 1$ and the vortex cores do not overlap. Then the energy of the system is purely electromagnetic and it is given by the sum of the supercurrent and the magnetic field energies

$$\mathcal{G}_L = \frac{2\kappa^2}{V} \int dV [(\mathbf{H} - \mathbf{H}_0)^2 + \kappa^2 |\mathbf{j}|^2]. \quad (3.5)$$

In the presence of L vortices, situated at $\boldsymbol{\rho}_i \{i = 1, 2, \dots, L\}$, the London equation can be written as

$$\mathbf{J} = \frac{d}{\kappa^2} (\mathbf{v} - \mathbf{A}), \quad (3.6)$$

where

$$\mathbf{v} = \sum_{i=1}^l [\Phi(|\boldsymbol{\rho} - \boldsymbol{\rho}_i|) - \Phi(|\boldsymbol{\rho} - (R/\rho_i)^2 \boldsymbol{\rho}_i|)], \quad (3.7)$$

with $\rho_i = (x_i, y_i)$ the position of the vortices, $\mathbf{J} = \int_0^d dz \mathbf{j} \simeq \mathbf{j}d$, where d is the thickness of the disk, and $\Phi(|\boldsymbol{\rho} - \boldsymbol{\rho}_i|) = \hat{z} \times (\boldsymbol{\rho} - \boldsymbol{\rho}_i) / |\boldsymbol{\rho} - \boldsymbol{\rho}_i|^2$. The vortex images at $(R/\rho_i)^2 \boldsymbol{\rho}_i$ appear in Eq. (3.7) in order to fulfill the boundary condition $\mathbf{J}(R) \cdot \hat{\rho} = 0$. Instead of writing Eq. (3.6) for the vector \mathbf{J} , one may use the streamline function, $g(\boldsymbol{\rho})$, related to the supercurrent by $\mathbf{J} = \nabla \times (\hat{z}g)$ ($g(\boldsymbol{\rho})$ can be regarded as a local magnetization in the thin film.) At the boundary $g(R, \phi) = \text{const}$, but, as the value of this constant is arbitrary, one can impose $g(R, \phi) = 0$. Therefore, Eqs. (3.6) and (3.7) can be expressed as

$$g(\boldsymbol{\rho}) = \frac{d}{\kappa^2} \left[\sum_{j=1}^L \ln \left(\frac{|\boldsymbol{\rho} - (R/\rho_j)^2 \boldsymbol{\rho}_j| \rho_j}{|\boldsymbol{\rho} - \boldsymbol{\rho}_j| R} \right) - \frac{H_0}{4} (R^2 - \rho^2) \right]. \quad (3.8)$$

Notice that Eq. (3.6) can also be understood as the limiting case of the GL equations if one considers $\Psi = 1$ and $\nabla \theta = \mathbf{v}$. Therefore, while vortices are well apart from each other (and also the boundary), there exists a relation between the streamline function defined above and the phase of the order parameter in the GL theory, i.e., one can define a complex function of which the real and imaginary parts are proportional to $g(\rho)$ and θ , respectively.

In the case $\lambda_{eff} = \lambda^2/d \gg \xi \gg d$, demagnetization effects can be neglected and one may write Eq. (3.5) as

$$\mathcal{G}_L = \frac{2\kappa^4}{Vd} \int d^2 \rho |\mathbf{J}|^2 = \frac{2\kappa^4}{Vd} \int d^2 \rho g(\boldsymbol{\rho}) \hat{z} \cdot \nabla \times \mathbf{J} = \frac{2\kappa^4}{Vd} \left[2\pi \sum_{i=1}^L g(\boldsymbol{\rho}_i) - H_0 \int d^2 \rho g(\boldsymbol{\rho}) \right], \quad (3.9)$$

where the integration is performed along the thin film plane, $z = 0$. Substituting Eq. (3.8) in this formula, and after some algebraic manipulation, the London energy is expressed by

$$\mathcal{G}_L = \left(\frac{2}{R} \right)^2 \sum_{i=1}^L \sum_{j=1}^L \ln \left(\frac{r_j |\mathbf{r}_i - \mathbf{r}_j / r_j|^2}{|\mathbf{r}_i - \mathbf{r}_j|} \right) - 2H_0 \sum_{i=1}^L (1 - r_i^2) + \frac{R^2 H_0^2}{4}, \quad (3.10)$$

where we used $\mathbf{r}_i = \boldsymbol{\rho}_i / R$ to simplify the notation.

The divergence in Eq. (3.10) can be removed by considering a cutoff, in which for $i \rightarrow |\boldsymbol{\rho}_i - \boldsymbol{\rho}_j| = a\xi$ (in not normalized units) and a is a constant. The final expression for the London energy can be written as

$$\mathcal{G}_L = \sum_{i=1}^L \left(\epsilon_i^{self} + \epsilon_i^{shield} + \sum_{j=1}^{i-1} \epsilon_{ij} \right) + \epsilon^{core} + \epsilon^{field}, \quad (3.11)$$

where

$$\epsilon_i^{self} = \left(\frac{2}{R}\right)^2 \ln(1 - r_i^2), \quad (3.12)$$

is the interaction energy between the i th vortex and the radial boundary of the superconductor

$$\epsilon_i^{shield} = -2H_0(1 - r_i^2), \quad (3.13)$$

represents the interaction between the i th vortex and the shielding currents, and

$$\epsilon_{ij} = \left(\frac{2}{R}\right)^2 \ln \left[\frac{(r_i r_j)^2 - 2\mathbf{r}_i \cdot \mathbf{r}_j + 1}{r_i^2 - 2\mathbf{r}_i \cdot \mathbf{r}_j + r_j^2} \right], \quad (3.14)$$

is the repulsive energy between vortices i and j . Finally, $\epsilon^{core} = (2/R)^2 L \ln(R/a)$ and $\epsilon^{field} = R^2 H_0^2 / 4$ are the energies associated with the vortex cores and the external magnetic field, respectively.

Notice that the above approach allows one to treat the vortices as point particles, which is valid when vortices are well separated from each other (typically valid for $H \leq 0.2H_{c2}$). Therefore, simulation techniques appropriate for systems of classical particles may be used in order to find, for example, the ground state of the system. In this sense, the vortex system behaves (in the London approximation) similar to a two-dimensional system composed of equally charged particles interacting through a repulsive logarithmic potential placed in a parabolic potential well. Nevertheless, there is a fundamental difference between these two systems: The vortex system is confined to a disk of radius R and the influence of the surface on the energy is clear from the terms containing vortex images, i.e., ϵ_i^{self} and ϵ_{ij} . Notice also that ϵ^{core} arises from the cutoff procedure and is therefore strongly dependent on the cutoff value $a\xi$ (we adopted $a = \sqrt{2}$ in the results shown below). The actual energy associated with vortex cores and with the spatial variation of the superconducting electron density ($|\psi(\boldsymbol{\rho})|^2$) should be evaluated by using the GL theory.

3.3 MOLECULAR-DYNAMICS SIMULATION

3.3.1 General introduction to the molecular-dynamics method

Molecular Dynamics (MD) is a computer simulation technique where the time evolution of a set of interacting particles is followed by integrating their equations of motion. Classical mechanics law, very often in the form of Newton's law, is used. Time integration is based on finite-difference methods, where the time is discretized on a finite grid, with the time step Δt as the distance between consecutive points on the grid. Knowing the positions and their time derivatives at time t' , the integration scheme gives the same quantities at a later time $t' + \Delta t$. By iterating the procedure, the time evolution of the system can be followed for long times. Hence, in contrast with the Monte Carlo(MC)

method, Molecular Dynamics is a deterministic technique, in the sense that given an initial set of positions and velocities, the subsequent time evolution is, in principle, completely determined.

In general, MD simulations calculate a trajectory in a $6N$ -dimensional phase space ($3N$ positions \mathbf{r} and $3N$ momenta \mathbf{p}). However, such trajectory is usually not particularly relevant by itself. Like MC methods, MD provides a set of configurations distributed according to some statistical distribution function, or statistical ensemble, depending on the specific equations of motion describing the system. Therefore, a measurement of a physical quantity A by MD simulations is simply obtained as an arithmetic average of the various instantaneous values assumed by that quantity during the runs:

$$\langle A(\mathbf{r}, \mathbf{p}) \rangle = \frac{1}{N} \sum_{m=1}^N A[\mathbf{r}(t_0 + m\Delta t), \mathbf{p}(t_0 + m\Delta t)], \quad (3.15)$$

where t_0 is the time at which the simulation starts and N is the total number of runs. In the limit of very long simulation times, for systems at equilibrium, one could expect the phase space to be fully sampled, and in that limit the averaging process would provide the “correct” results.

MD is a very useful tool and is nowadays indispensable for studying the properties of liquid and gas systems, defects in crystals, surfaces; it provides information in electronic and transport properties, biomolecules and non-equilibrium processes. It can also be used for the optimization of structures overcoming local energy minima (together with the simulated annealing technique).

Generally, a MD simulation integrates the differential equations:

$$m_i \frac{d^2 \mathbf{r}_i}{dt^2} = \mathbf{F}_i(\mathbf{r}_1, \dots, \mathbf{r}_n, \frac{d\mathbf{r}_1}{dt}, \dots, \frac{d\mathbf{r}_n}{dt}), \quad (3.16)$$

for each particle i of the system, constituted by n particles, with m_i the mass of the i -th particle and \mathbf{F}_i the force acting upon it. When the forces are independent of the velocity, which is the case for a large variety of systems of interest, and when they can be obtained as the gradient of a potential:

$$\mathbf{F}_i = \nabla_{\mathbf{r}_i} V(\mathbf{r}_1, \dots, \mathbf{r}_n), \quad (3.17)$$

the mechanical energy is conserved or, stated differently, the system of N particles evolves in the microcanonical ensemble. In this case the knowledge of the potential V is the only requirement to start a MD simulation. When the forces acting on the particles cannot be simply deduced from a potential or when the evolution takes place in a different thermodynamical ensemble, either the equation of motions should be modified or the time integration algorithm should be slightly changed with the introduction of some intermediate steps which appropriately rescales the observable in order to reproduce the correct dynamics. In these cases, some forces are derived from a potential

and other additional effects are included. Hence, the choice of the potential is a key point in every MD simulation. Together with the time integration strategy, they are the heart of MD techniques. The development of accurate potentials represents an important research line.

3.3.2 Langevin molecular dynamics

The equations of motion in the Newton form preserve the mechanical energy. When the system of particles does not exchange energy with the environment, they describe correctly its evolution. When the system can exchange energy with the environment or different degrees of freedom are present, the equations of motion should be modified in order to get the correct dynamics. In the case that the evolution of the system is represented by the canonical distribution of probability, which means that the system is in thermal equilibrium with a heat bath, the motion of the particles is properly described by Langevin equations.

The Langevin equation is a stochastic differential equation in which two force terms are added to Newton's second law in order to approximate the effects of neglected degrees of freedom: one term represents a frictional force, proportional to the velocity, and the other one a random force. The friction removes kinetic energy from the system, while the random force adds kinetic energy to the system. To generate a canonical ensemble, the friction and random force have to obey the fluctuation-dissipation theorem.

The formal equations of motion for Langevin dynamics for a one-dimensional system are:

$$m dv = -m\gamma v dt + f(r)dt + dW, \quad (3.18)$$

$$dr = v dt, \quad (3.19)$$

where γ is the friction constant and W is a stochastic process, known as Wiener process. It has the following properties:

1. $W(t)$ is normally distributed for $t \geq 0$;
2. $\langle W(t) \rangle = 0$ for $t \geq 0$;
3. $W(0) = 0$

By specifying the spread of the distribution of $W(t)$, the required ensemble can be generated, in particular with:

$$\langle W(t)W(t+\tau) \rangle = 2m\gamma k_B T \tau, \quad (3.20)$$

the canonical ensemble is generated for the temperature T . The last expression is simply the formulation of the fluctuation-dissipation theorem in the canonical ensemble.

The differential form for the Langevin equations in Cartesian coordinates is:

$$m_i \frac{d^2 \mathbf{r}_i}{dt^2} = -m_i \sum_j \Gamma_{ij} \frac{d\mathbf{r}_i}{dt} + \mathbf{f}_i(\mathbf{r}_i) + \xi_i, \quad (3.21)$$

where the subscript i denotes the particle number, Γ_{ij} is a 3×3 friction matrix, $\mathbf{f}(\mathbf{r}) = -\nabla V(r)$ and ξ_i is a random force, often called noise. In most cases the friction matrix is diagonal and isotropic, which simplify the form of Eq. (3.21) to:

$$m_i \frac{d^2 \mathbf{r}_i}{dt^2} = -m_i \gamma_j \frac{d\mathbf{r}_i}{dt} + \mathbf{f}_i(\mathbf{r}_i) + \xi_i, \quad (3.22)$$

with γ_i the friction coefficient of the i -th particle.

Without memory of the history of the system, the noise is not correlated in time and gaussian distributed. The correlation is, thereby, given by:

$$\langle \xi_{ik}(t) \xi_{jl}(t + \tau) \rangle = 2m_i \gamma_i k_B T \delta_{ij} \delta_{kl} \delta(\tau), \quad (3.23)$$

where k and l indicate the Cartesian vector components, δ_{ij} is the Kronecker delta and $\delta(\tau)$ is the Dirac delta function.

The Langevin molecular Dynamics is a very effective method to study the dynamics of vortices, driving by an external force, moving on different potential energy landscapes. It was successfully applied to study, *e.g.* the commensurate and incommensurate vortex states [43], the dynamic phases of vortex plastic flow [44, 45] in superconductors with periodic pinning arrays and the dynamics of vortices and the enhancement of the critical current in quasiperiodic array of pinning sites [46].

3.4 NUMERICAL PROCEDURE

From part (3.2) and Ref. [47], the choice $a = \sqrt{2}$ makes the London energy agree well with the Ginzburg-Landau (GL) energy if a contribution $e' \approx -1 + 3L/R^2$ is added to the London energy. However, ϵ^{core} and ϵ^{field} are only necessary in order to determine the actual state with lowest energy. Since these terms do not depend on the vortex positions (in the London approach), they do not contribute to the results discussed in the present work.

From the expression of the free energy of Eqs. (3.11) – (3.14), we can obtain the force acting on each vortex, by using $-\nabla_k \mathcal{G}(\boldsymbol{\rho}_i, \boldsymbol{\rho}_j)$, where $-\nabla_k$ is the gradient with respect to the coordinate $\boldsymbol{\rho}_k$. This yields a force per unit length,

$$\mathbf{F}_i = \mathbf{F}_i^s + \sum_k \mathbf{F}_{i,k}^{int}, \quad (3.24)$$

in units of $H_c^2 \xi / 8\pi$, where the summation runs over k from 1 to L , except for $k = i$. The first term describes the vortex interaction with the current induced by the external field and with the interface,

$$\mathbf{F}_i^s = \left(\frac{2}{R}\right)^3 \left(\frac{1}{1-r_i^2} - \frac{H_0 R^2}{2}\right) \mathbf{r}_i. \quad (3.25)$$

The second term is the vortex-vortex interaction

$$\mathbf{F}_{i,k}^{int} = \left(\frac{2}{R}\right)^3 \left(\frac{\mathbf{r}_i - \mathbf{r}_k}{|\mathbf{r}_i - \mathbf{r}_k|^2} - r_k^2 \frac{r_k^2 \mathbf{r}_i - \mathbf{r}_k}{|r_k^2 \mathbf{r}_i - \mathbf{r}_k|^2} \right). \quad (3.26)$$

The above equations allow us to treat the vortices as particles and resemble the forces of interaction of a two-dimensional system composed of charged particles with pairwise $1/r$ repulsion, confined to some potential.

To investigate the different vortex configurations, we first have to find the stable configurations. This was accomplished by performing a molecular dynamics (MD) simulation starting from randomly distributed initial vortex states. The final configurations were found after typically 10^6 MD steps. In order to find the ground state (or states with energies very close to it) this trial procedure was repeated several times for the sample with same radius and same vorticity (100 times each), we count the times each configuration appears, calculate the total energy every time and take the average energy for each vortex configuration. By comparing these energy states of different configurations, we tried to find the stable states for a certain sample radius and applied magnetic field, in other words, the states with lowest total energy.

The MD simulation was performed by using the Bardeen-Stephen equation of motion [48]

$$\eta \frac{d\rho_i}{dt} = \mathbf{F}_i, \quad (3.27)$$

where i represents the i th vortex, η is the viscosity coefficient $\eta \sim \Phi_0 H_{c2} / \rho_n c^2$, with ρ_n being the normal-state resistivity. The time integration was accomplished by using the Euler method, but using sufficiently small time steps δt in order to assure small vortex displacements between two consecutive steps.

Notice that both \mathcal{G} and the forces acting on the vortices diverge at the disk edge, which arises due to the failure of the London limit when $\rho > R - \xi$. To avoid numerical difficulties during the MD simulation, a vortex leaves the disk whenever it was at a distance less than ξ from the disk edge.

4

Vortex configurations in mesoscopic SC disks

4.1 FORMATION OF VORTEX SHELLS

Vortex configuration in mesoscopic superconducting disk have been earlier discussed in works (Ref.[37]), where they were calculated using the Ginzburg-Landau equations. Here we study vortex configurations in mesoscopic superconducting disks using the London approach and Molecular Dynamics. We investigate the formation of vortex shells recently observed in the experiment [42] and we obtained in our calculations the states [e.g. (2,7)] detected in the experiment as ground state of the system which have not been found in earlier calculations. Thus, using the results of our calculations we have added the missing states in the “periodic table” describing the formation of vortex shells in mesoscopic superconducting disks, in agreement with a recent experiment [42].

4.1.1 Vortex configurations for different vorticity numbers

4.1.1.1 The evolution of the vortex configurations When the vorticity of the sample is increased from $L = 1$ to $L = 4$, the vortex configurations evolve with increasing applied magnetic field as follows (see Figs. 4.1, 4.2): starting from a Meissner state without vortex, then one appears in the center, then two symmetrically distributed in the disk. Further increasing field results in the formation of triangular and square like vortex patterns in the sample, and, finally, a first vortex shell is formed consisting of 5 vortices. When the vorticity L increases from 5 to 6, a vortex appears in the center of the disk

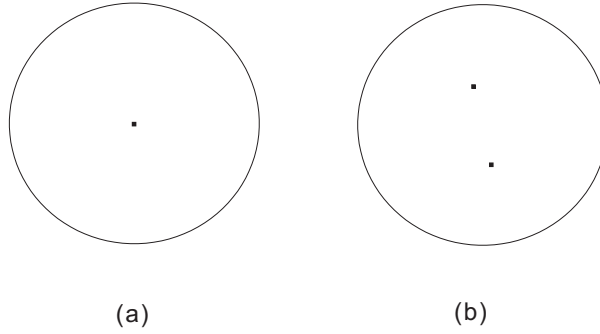


Fig. 4.1 The vortex configuration for $L=1$ (a) and $L=2$ (b)

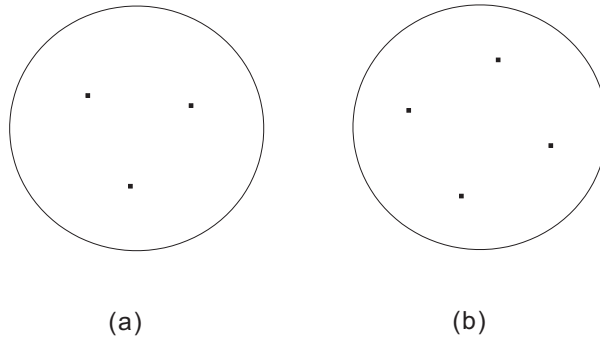


Fig. 4.2 The vortex configuration for $L=3$ (a) and $L=4$ (b)

and therefore forms a two shells configuration of vortices $(1,5)$, compared with a circle like distribution of 5 vortices. This two shell configuration of vortices remains for $L = 7$, $L = 8$, till $L = 9$, and in this process the newly generated vortices are added to the outer shell to form $(1, 6)$, $(1, 7)$ respectively.

The inner shell begins to grow at $L = 9$ to form a configuration of $(2, 7)$, with next two states having 2 vortices in the center, in agreement with the experiment of Ref. [42]. Note that in earlier theoretical works on vortices in mesoscopic superconducting disks, a configuration of $(1,8)$ was predicted [37], which was not observed in experiments as a stable state [42]. The multivortex state with two vortices in the center and the other vortices on the outer shell can exist till $L = 14$.

When $L > 14$, the inner shell begins to grow again till $L = 16$, which means the newly nucleated vortex will be generated in the center, while the number of vortices on the outer shell stays the same. Those configurations, from our calculation, are $(3, 11)$ $L = 14$, $(4, 11)$ $L = 15$, and $(5, 11)$ $L = 16$.

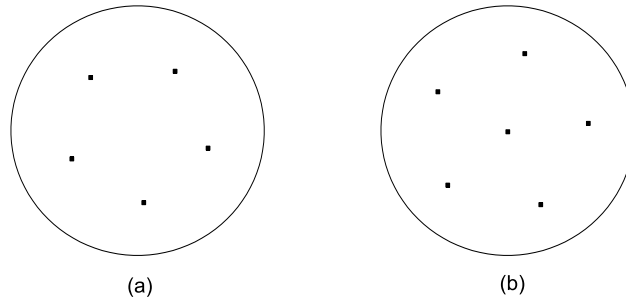


Fig. 4.3 The vortex configuration for $L=5$ (a) and $L=6$ (b).

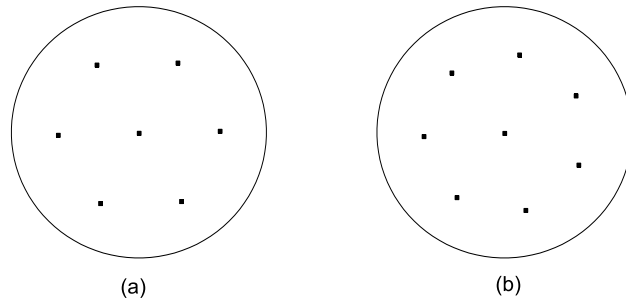


Fig. 4.4 The vortex configuration for $L=7$ (a) and $L=8$ (b).

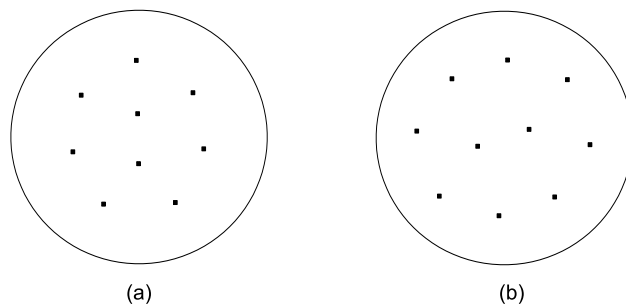


Fig. 4.5 The vortex configuration for $L=9$ (a) and $L=10$ (b).

At $L = 17$, a third shell appears with one vortex formed in the center. The next three vortices are added to the outermost shell, after which all three shells grow intermittently till $L = 32$. And the fourth shell appears at $L = 33$ in the form of one vortex in the center.

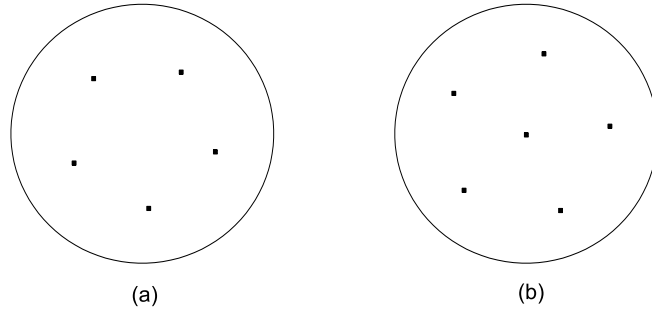


Fig. 4.6 When L changes from 5 to 6, a vortex appears in the center of the disk, which forms a two shell structure configuration.

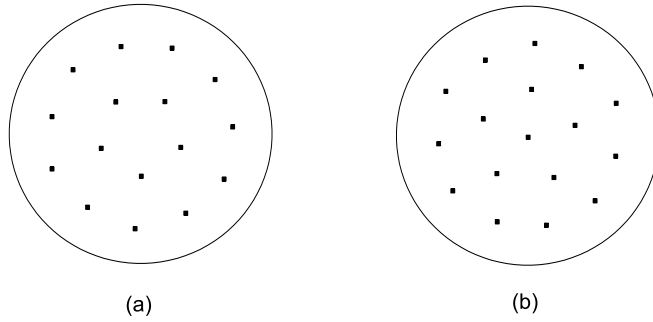


Fig. 4.7 When L changes from 16 to 17, the vortex configuration turns out to be $(1,5,11)$, which brings out the third shell.

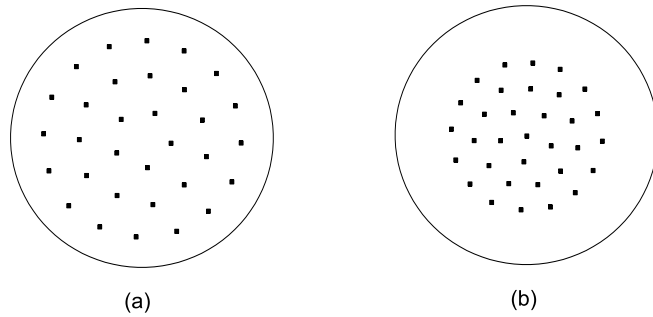


Fig. 4.8 Also for the vorticities changing from 32 to 33, the configuration change from $(5,11,16)$ to $(1,5,11,16)$, and the fourth shell structure forms.

Thus we find the same phenomenon as in the experiment [42], that a new shell forms when the vortex number changes from 5 to 6 as (5) to $(1,5)$, from 16 to 17 as $(5,12)$ to $(1,5,11)$, 32-33 for $(5,11,16)$ - $(1,5,11,16)$ as illustrated in Figs. 4.6-4.8.

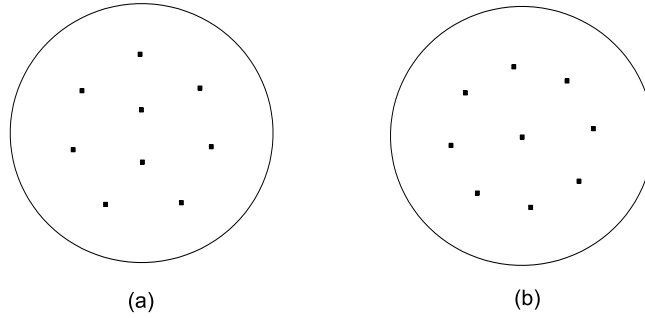


Fig. 4.9 The configurations for $L = 9$ (2,7) (a) and (1,8) (b).

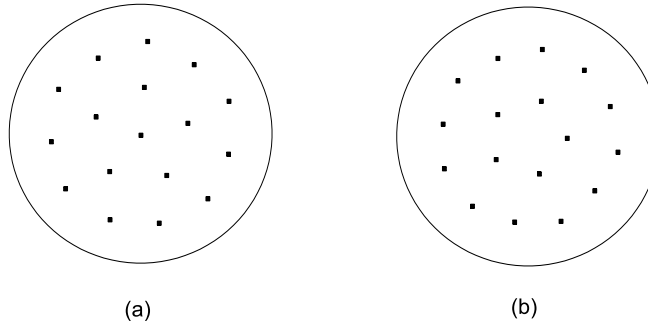


Fig. 4.10 The configurations for $L = 17$ (1,5,11) (a) and (5,12) (b).

4.2 THE GROUND STATE OF THE VORTEX SYSTEM

4.2.1 The possible configurations for a given vorticity L

Let us consider the case of $L = 9$. From our calculations, it follows that two configurations (1,8), and (2,7) are possible for the same vorticity $L = 9$. They are shown in Fig. 4.9. Here, we obtain the result that the configuration (2,7) is the stable state for radius $R = 50\xi$, in agreement with Ref. [42]. Note that configuration (2,7) was found as a ground state for charged particles [29]. While in early theoretical work [37], (1,8) was found as a ground state for radius $R = 6\xi$.

In the case of $L = 17$, a competition of two different configurations was also found. In Fig. 4.10, configuration (1,5,11)(a) was found as a three shell distri-

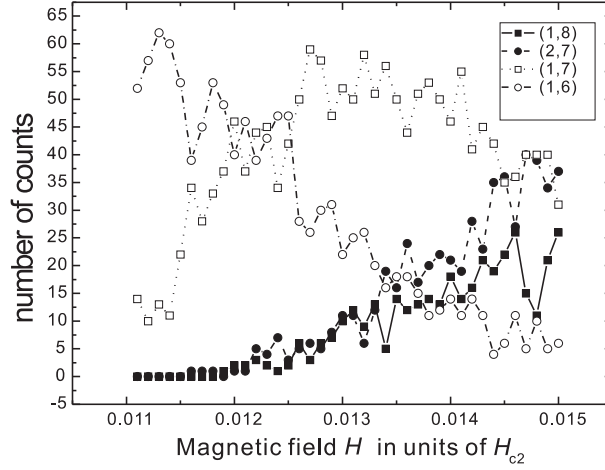


Fig. 4.11 The statistical result for different vortex configurations in a disk with radius $R = 42\xi$ and $L = 9$.

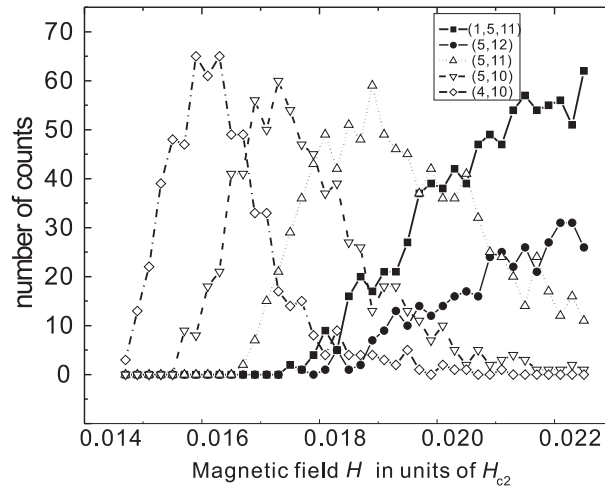


Fig. 4.12 The statistical result for different vortex configurations in a disk with radius $R = 47\xi$ and $L = 17$.

tribution for a minimum L . While it is possible to find configuration (5,12)(b) for lower magnetic field or larger radius of the sample.

4.2.2 The ground and metastable states

4.2.2.1 Statistical study of different vortex states In the experiments [42], vortex configurations were monitored in large arrays of similar mesoscopic disks (dots). This allowed them to study the statistics of the appearance of different vortex configurations in practically the same disk at the same conditions. The results show that, e.g., in disk with radius $R = 1.5\mu m$ and magnetic field $H_0 = 60Oe$, configuration (2,8) for $L = 10$ appears more frequently. Other configurations for the same total vorticity $L = 10$, e.g., configuration (3,7) appears only in a few cases. Interestingly, not only various configurations with the same total vorticity $L = 10$ appear, but also vortex states with $L = 9$ (2,7) as well as two modifications of states (1,8). This statistical study provides a valuable indirect information about the ground-state and metastable states: those states which appeared in most cases were treated as ground-state configurations. We perform similar investigation of the statistics of the appearance of different vortex states in our calculations. One hundred randomly distributed initial states were chosen for our statistical study, with $R = 42\xi$ and magnetic field varied from 0.013 to 0.017 (in units of H_{c2}).

During the simulation we counted how many times the configurations (1,8) and (2,7) appeared when magnetic field increases, see Fig. 4.11. At low magnetic field 0.013, the disk cannot accommodate 9 or even 8 or 7 vortices, so the number of configurations (1,8) and (2,7) is zero, and in most cases we obtain, configurations (1,7) or (1,6) for $L = 8$, and $L = 7$ respectively. As the magnetic field increases, the number of configurations (1,8) and (2,7) increase, and at the same time the number of configuration (1,6) and (1,7) decreases. Similar simulation is done for a disk with radius $R = 47\xi$ and $L = 17$. The configurations of (4,10) $L = 14$, (5,10) $L = 15$, (5,11) $L = 16$ and (1,5,11), (5,12) for $L = 17$ become to be the dominant, see Fig. 4.12, as the magnetic field increases. Also two configurations (1,5,11) and (5,12) appear at the same time for $L = 17$, while (1,5,11) always is the dominant one.

From our statistical result, the possibility to get configuration (2,7) is always higher than to get configuration (1,8).

4.2.2.2 The Randomly Generated initial states It is worth to note here that for the statistical study, it is very important to investigate the influence of the initial conditions on the obtained vortex distributions. In this respect, one should ensure that the initial vortex distribution is really random, and also to avoid unexpected metastable states by properly performing the annealing of the initial state.

To exclude the possibility that some initial distributions of the vortex can result in a certain preferable configurations in MD simulation, it is very important to introduce a “real” random generator.

Two different generators were used in our simulations, and results are compared to each other. One is the standard random generator from “Numerical Recipe” [49]. The code for the other one is the following.

How to generate these vortices randomly in a disk sample? It is very easy to make a mistake by mapping the random generated number simply to the region $(0-R_0)$ and $(0-2\pi)$, and set these two random numbers as indices for radius and angle of a vortex, respectively. In this case, the vortex density will be higher in the center of the sample than in the outer area. The correct way is as follows:

```

REAL rand
INTEGER irand
INTEGER*4 timeArray(3)
ia=16807
ic=2147483647
iq=127773
ir=2836
CALL itime(timeArray)
irand = rand ( timeArray(1)+timeArray(2)+timeArray(3) )
iseed=rand(0)*FLOAT(ic)
ih=iseed/iq
il=MOD(iseed,iq)
it=ia*il-ir*ih
IF(it.GT.0) THEN
iseed=it
ELSE
iseed=ic+it
END IF
ranf=iseed/FLOAT(ic)

```

(i) first randomly generate a vortex in an square, whose border is twice the disk radius,

(ii) secondly, remove the vortex that fall outside the disk, keep the one which is inside and count it till the vorticity reached the number required in our simulation.

4.2.2.3 Temperature effect and metastable state In addition to the minimization routines of the MD approach, we also performed simulations with varying temperatures. We employed a thermal contribution to the Bardeen-Stephen equation of motion [48]

$$\eta \frac{d\rho_i}{dt} = \mathbf{F}_i + \Gamma_i, \quad (4.1)$$

where Γ_i is a thermal fluctuation force. The simulations gave us an insight into the time-dependent dynamics of the system, particularly for studying the stable-metastable states. For this purpose, we started with a state which

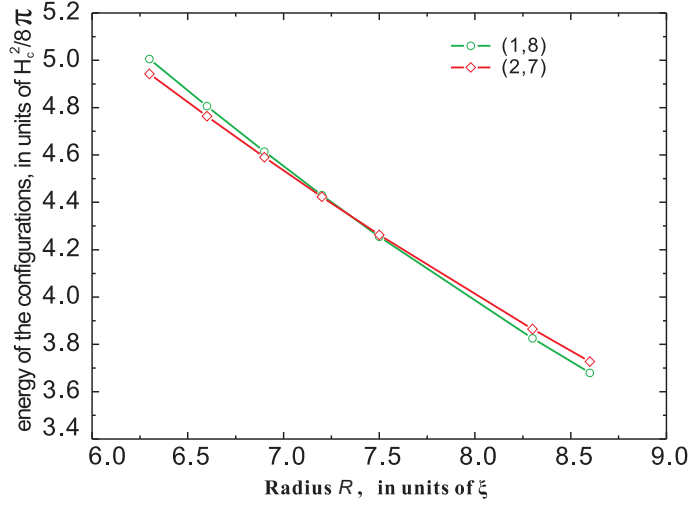


Fig. 4.13 The energy curve of two configurations (1,8) and (2,7) for flux $\Phi = 68.7$ (in units of $H_{c2}\xi^2$).

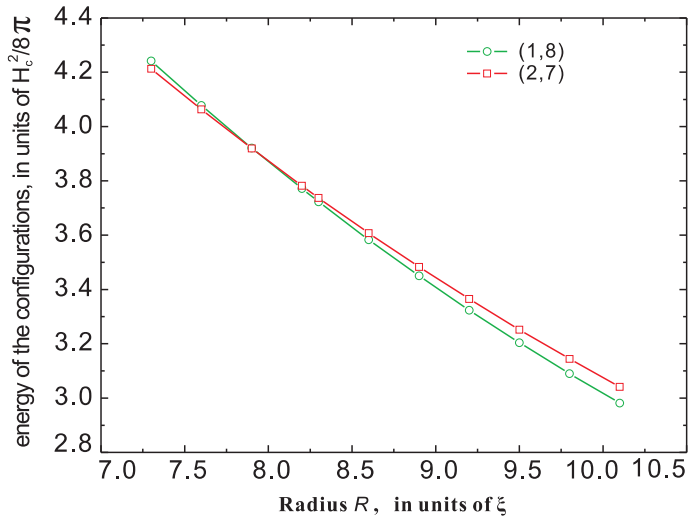


Fig. 4.14 The energy curve of two configurations (1,8) and (2,7) for flux $\Phi = 71.2$ (in units of $H_{c2}\xi^2$).

was local stable, and then apply an initial temperature or a shake to the system to free the configuration out of a local minimum. After that the system was cooled down at a high exponential sweep rate [approximately $T(t) = \exp(-t)T_0$, where T_0 was the initial temperature].

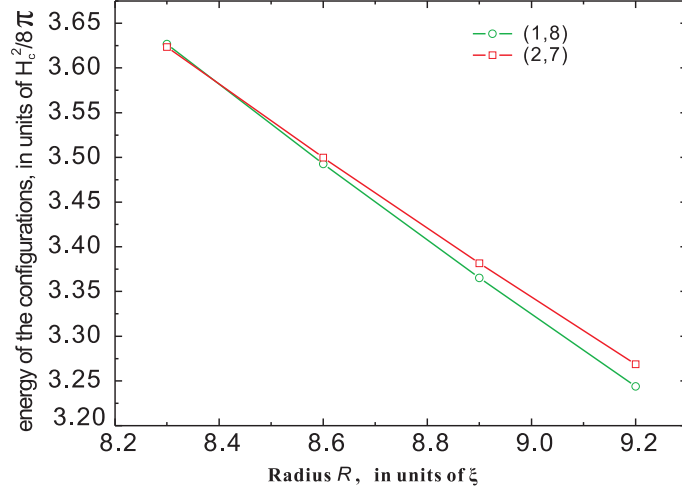


Fig. 4.15 The energy curve of two configurations (1,8) and (2,7) for flux $\Phi = 73.7$ (in units of $H_{c2}\xi^2$).

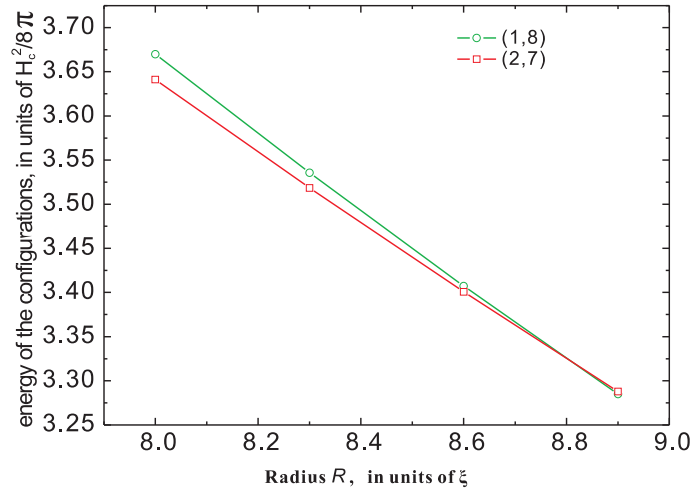


Fig. 4.16 The energy curve of two configurations (1,8) and (2,7) for flux $\Phi = 76.3$ (in units of $H_{c2}\xi^2$).

4.3 H - R PHASE DIAGRAM

4.3.1 Energy study of different vortex states

Using the expressions (3.12)-(3.14) for the energies in the London approximation, we obtain

$$\epsilon_i^{self} = \left(\frac{2}{R}\right)^2 \ln(1 - r_i^2),$$

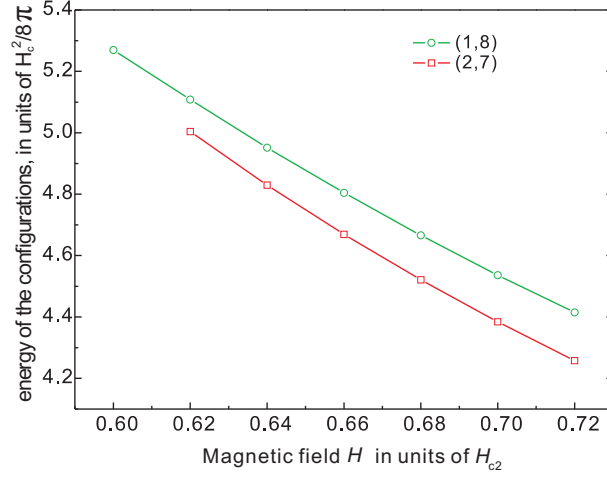


Fig. 4.17 The energy curve of two configurations (1,8) and (2,7) for a sample with $R = 6\xi$.

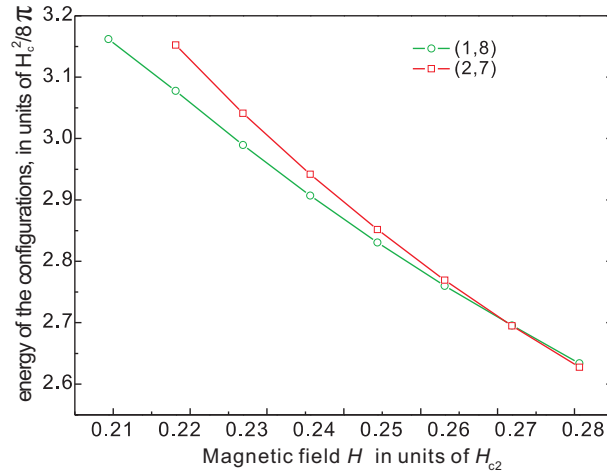


Fig. 4.18 The energy curve of two configurations (1,8) and (2,7) for a sample with $R = 10\xi$.

as the interaction energy between the i th vortex and the radial boundary of the superconductor,

$$\epsilon_i^{shield} = -2H_0(1 - r_i^2).$$

represents the interaction between the i th vortex and the shielding currents, and

$$\epsilon_{ij} = \left(\frac{2}{R}\right)^2 \ln \left[\frac{(r_i r_j)^2 - 2\mathbf{r}_i \cdot \mathbf{r}_j + 1}{r_i^2 - 2\mathbf{r}_i \cdot \mathbf{r}_j + r_j^2} \right].$$

is the repulsive energy between vortices i and j , $\epsilon^{core} = (2/R)^2 L \ln(R/a)$ and $\epsilon^{field} = R^2 H_0^2/4$, where $a = \sqrt{2}$ (Ref. [47]). We calculate the energy of possible vortex configurations for certain value of applied magnetic field and sample radius.

We can see in Fig. 4.17, that for the sample radius $R = 6\xi$, the energy of the configuration (1,8) is always lower than that of the configuration (2,7). Note that for radius $R = 6$ the energies of both configurations decreases within the chosen range of the magnetic field. The vortex state (1,8) has always a lower energy and thus is the ground state of the system (compare to Ref. [37]).

4.3.2 Phase diagram

For convenient comparison, we study the energies of configurations (1,8) and (2,7) in disks with radius ranging from $R = 4\xi$ up to $R = 50\xi$. We change the radius of the specimen, and at the same time keep the flux passing through the specimen $\Phi \sim H_0$ the same, in order to keep a preserved vorticity L in the disk. Here Φ is the flux passing through the specimen, H_0 is the applied magnetic field, S is the surface of the specimen which can be expressed as πR_0^2 .

For each point with different H and R in the figure, we calculated the average energy over all the configurations (1,8) or (2,7) using Eqs. (3.12)-(3.14). The flux through the specimen was changed by small steps $2.54 H_{c2} \cdot \xi^2$. The results of our calculation of the energy of the vortex configurations (1,8) and (2,7) as a function of radius are presented in Figs. 4.13-4.16. From these figures, a relationship was found between the critical magnetic field/radius where the energy of those states are the same. As we can see in Figs. 4.13-4.16, when the flux increased from $63.6 \sim 101.7$ (in the unit of $H_{c2} \cdot \xi^2$), the critical magnetic field for the crossing point decreased, while at the same time the critical radius increased. The crossing points were plotted with respect to the applied magnetic field H_0 and the specimen radius R , see Fig. 4.20 and Fig. 4.21 (magnified picture of the phase boundary part). This constitutes the phase boundary between the configurations (2,7) and (1,8).

For small radius $R < 7\xi$, for example $R = 6\xi$, as Fig. 4.20 demonstrates, the energy of the configuration (2,7) appears to be always lower than that of configuration (1,8). The total energy for both curves decreases with increasing the magnetic field. Notice that the magnitude of the energy change of state (2,7) is slightly longer than that of the state (1,8).

For the specimen with radius between 7ξ and 12ξ , such as $R = 10\xi$, see Fig. 4.18, the configuration (1,8) has a lower energy than configuration (2,7) for low applied magnetic field. For increasing magnetic field, up to $H_0 \leq 0.27$, the energy of configuration (2,7), is still higher than that of the vortex state (1,8). When the magnetic field reaches some critical value $H_0 = 0.27$, these two configurations have the same energy. After that point, the energy of (2,7) becomes lower than that of (1,8) as the magnetic field increases, until these two configurations are no longer stable in the specimen.

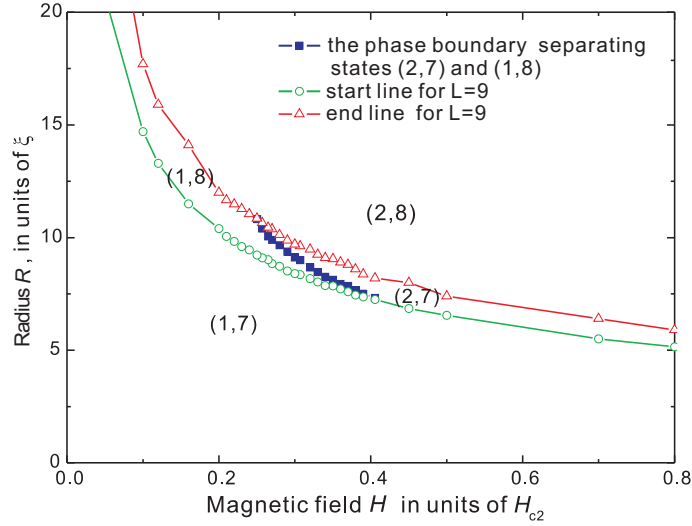


Fig. 4.19 Phase diagram.

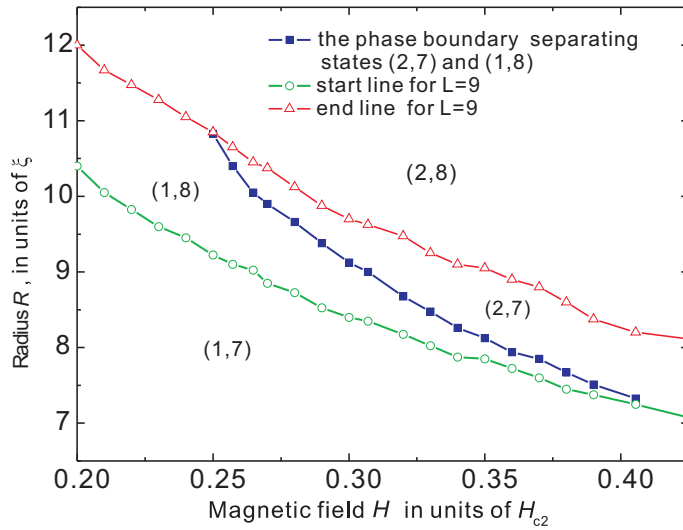


Fig. 4.20 Magnified area of phase diagram of Fig. 4.19.

For large radius, here we consider $R = 15\xi$ Fig. 4.21, and $R = 50\xi$ Fig. 4.22, configuration (1,8) always has a lower energy than that of the state (2,7), for the considered range of magnetic field. As we can see from Fig. 4.21 the difference between the energies of states (2,7) and (1,8) becomes smaller for increasing field. To better see this tendency. The energy curves are supposed to cross for higher values of the magnetic field outside the region shown in the

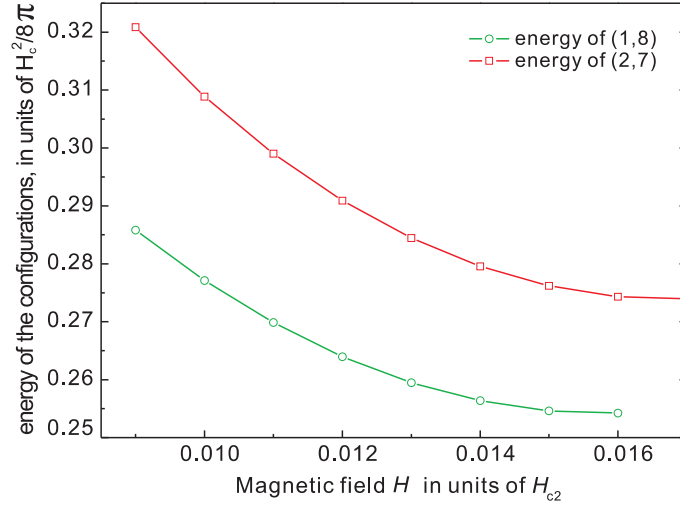


Fig. 4.21 The energy of two configurations (1,8) and (2,7) for $R = 50\xi$.

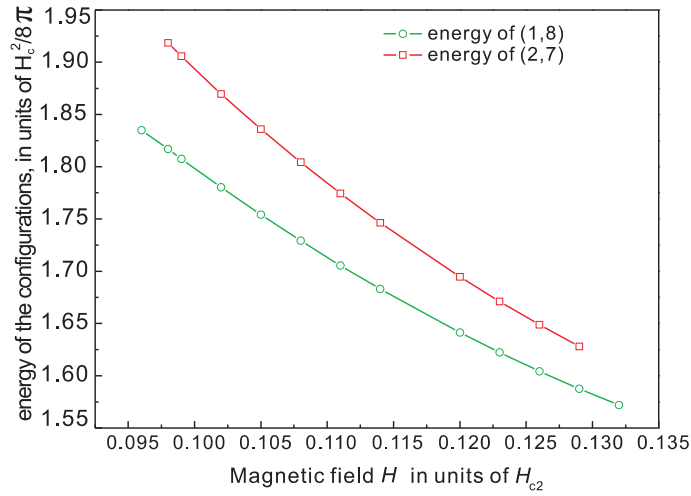


Fig. 4.22 The energy of two configurations (1,8) and (2,7) for $R = 15\xi$.

figure. However, when the magnetic field is too large, the system will generate another vortex to form configuration (2,8) with total vorticity $L = 10$ to keep the superconducting states from being destroyed.

So from these results, we can conclude that the competition between the two configurations (2,7) and (1,8), only exists for disks whose radius range from $R = 7\xi$ to $R = 12\xi$. In this case, both configurations can be the ground state. But for a large disk, $R > 12\xi$, the configuration (1,8) has always a

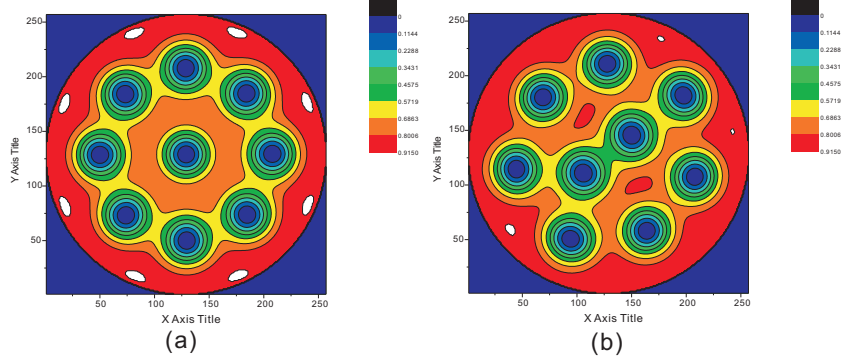


Fig. 4.23 Contour plots of the Cooper-pair density of the (1,8)-state at $R = 8.2\xi$ (a), the (2,7)-state at $R = 8.3\xi$, in the condition of applied magnetic field $H_0 = 0.35H_{c2}$. Blue (red) regions correspond to low (high) Cooper-pair density.

lower energy and is the ground state; while for smaller radius $R < 7\xi$, the configuration (2,7) always has a lower energy and becomes the ground state.

4.3.3 Compare with the GL simulation

Ginzburg-Landau equations also are used to calculate the free energy and find the ground state (Ref. [37]). The expression for dimensionless Gibbs free energies of the different vortex configurations is following:

$$\mathcal{G} = V^{-1} \int_V [2(\vec{A} - \vec{A}_0) \cdot \vec{j}_{2D} - |\Psi|^4] d\vec{r}, \quad (4.2)$$

By comparing the dimensionless Gibbs Free energies of the different vortex configurations, we find the ground state. In this way, we can find the same competition for two configurations (2,7) and (1,8) in the specimen with vorticity $L = 9$ as what we found in Molecular dynamic method. Applied magnetic field and samples' size were chosen corresponding to the MD process.

Samples with different radius were examined for a fixed external magnetic field $H = 0.35H_{c2}$. For disk with radius $R = 8.2\xi$, our calculation leads to the ground vortex state (1,8) with lower energy state. When the radius of the size increased, the energy of (1,8) state kept being lower till $R = 8.25\xi$, after which the configuration of (2,7) became the ground state, see in Fig. 4.23. And this critical point with radius of $R = 8.25\xi$ and applied magnetic field of $H = 0.35H_{c2}$ therefore contributed to the phase boundary in the phase diagram.

5

Conclusion

In this Thesis, I have studied the vortex configurations in mesoscopic superconducting disks within the London approach, using the Molecular-Dynamics simulations of Langevin-type equations of motion.

The educative and methodological aims of this work were to study the effects of vortex confinement in mesoscopic superconductors and the specific methods used for the description of vortex states in those systems, as well as to learn about early works and achievements in this field. In this respect, a special emphasis was made on the discussion of various vortex states in mesoscopic disks, i.e., multivortex states and giant vortex states, in particular, the theoretical prediction of these vortex states and their experimental realization. We also discussed the appearance of vortex molecules and vortex lattices in mesoscopic superconductors.

One of the important motivations of this work were very recent experiments [42] on the direct observation of vortex *shell* structures in mesoscopic Nb disks by means of Bitter decoration technique. It was shown in those experiments, that in disks with vorticity changing from $L = 1$ to 40, vortices fill the disk according to specific rules, forming well-defined shell structures, when the applied magnetic field gradually increases. They analyzed in detail the formation of these shells which resulted in a “periodic table” of formation of shells similar to the periodic table of elements. It was shown that many of the experimentally observed configurations agree with those earlier predicted in theory for mesoscopic superconducting disks. At the same time, some of the configurations which were observed in these experiments were not found earlier in vortex systems (although they were shown to appear in systems of charged particles and in superfluids).

We studied numerically the formation of vortex shells in mesoscopic superconducting disks. We found numerically the rules according to which the shells are filled with vortices for increasing applied magnetic field. In particular, it was shown in our calculations, that for the vortex configurations with the number of vortices up to $L = 5$, the vortices form one single shell. The formation of a second shell starts from $L = 6$. Similarly, the formation of a third shell starts for $L = 17$, and of a fourth shell at $L = 33$. These theoretical findings are in agreement with the results of the experimental observations of Ref. [42]. Moreover, we have found in our calculations those states which appear in the experiments as ground-state-energy states but which were previously not obtained in calculations. Thus, we have filled the missing states in the “periodical table” of formation of vortex shells in mesoscopic disks. We studied in detail the regions of parameters where these states appear, and made a comparison to previous theoretical works.

We studied the possibility of the existence of ground-state-energy states and metastable states possessing the same total vorticity L in disks. For this purpose, we used two methods. First method is based on studying the statistics of the appearance of different states, similarly to what was done in the experiment when measurements were performed on large arrays of practically the same dots (mesoscopic disks), and then the numbers of counts of all competing states were analyzed. The most frequently appeared state was considered as the ground state. We performed a similar statistical study for vortex configurations with the same vorticity L as well as for neighboring states, i.e., with close values of L , and we followed the evolution of them with changing radius of the disk and applied magnetic field. *Second* method is based on a direct comparison of the energies of the superconducting states with different vortex distributions. Using both these methods, we showed that, e.g., for a certain set of parameters, state (2,7) with total vorticity $L = 9$ becomes the ground state of the system while the competing state (1,8) is a metastable state, in agreement with the recent experiment. We have found these regions of parameters, and on that basis we obtained the region of existence of states with total vorticity $L = 9$, and we found the line within this region which separates the subregions where either state (2,7) or state (1,8) is the ground state. Thus, we found the phase diagram for the states $L = 9$ in the space “radius of the disk R – applied magnetic field H_0 ”.

Thus, in our work we studied the vortex configurations and the formation of shells in mesoscopic superconducting disks. Our results have contributed to the “periodical table” for vortex shells in disks and are in agreement with recent experimental observations of vortex shells in mesoscopic superconducting disks.

References

1. J. G. Bednorz and K. A. Müller, *Z. Phys. B* **64**, 189 (1986)
2. S. N. Putilin, E.V. Antipov, A.M. Abakumov, M.G.Rozova, K.A. Lokshin, D.A. Pavlov, A. M. Balagurov, D.V. sheptyakov, M. Marezio, *Physica C* **338**, 52 (2000).
3. W. Meissner and R. Ochsenfeld, *Naturwissenschaften* **21**, 787 (1933).
4. L.D. Landau and E.M. Lifshitz, *Statistical Physics*, 3rd edn., part 1 (pergamon Press, Oxford, **1980**).
5. M. Tinkham, *Introduction to superconductivity* (McGraw-Hill, London, **1975**).
6. P.G de Gennes, *Superconducting of Metals and Alloys* (Benjamin, New York, **1966**).
7. A. C. Rose-Innes and E. H. Rhoderick, *Introduction to Superconductivity* (Pergamon Press, Oxford, **1969**).
8. J. Pearl, *Appl. Phys. Lett.* **5**, 65(1964).
9. E. H. Brandt, *Braz. J. Phys.* **32**, 675 (2002).
10. W.A. Little and R. D. Parks, *Phys. Rev. Lett.* **9**, 9 (1962); *Phys. Rev.* **133**, A97 (1964).

11. J. Berger and J. Rubinstein, Phys. Rev. Lett. **75**, 320 (1995); Phys. Rev. B **56**, 5124 (1997).
12. I.R. Coddington, *Vortices in a Highly Rotating Bose Condensed Gas*, Ph.D thesis (2004)
13. V.A. Schweigert and F. M. Peeters, Phys. Rev. B **57**, 13 817 (1998).
14. P.S. Deo, V. A. Schweigert, F.M. Peeters, and A. K. Geim, Phys. Rev. Lett. **79**, 4653 (1997).
15. V.A. Schweigert, F. M. Peeters, and P.S. Deo, Phys. Rev. Lett. **81** 2783 (1998).
16. B.J. Baelus, *Vortex Matter in Mesoscopic Superconductors*, Ph.D thesis (2002).
17. P.S. Deo, F.M. Peeters, and V. A. Schweigert, Superlattices Microstruct. **25**, 1195 (1999).
18. J.J. Palacios, Phys. Rev. B **58**, R5948 (1998); E. Akkermans and K. Mallick, J. Phys. A **32**, 7133 (1999).
19. G. Dolan, J. Low Temp. Phys. **15**, 133 (1974).
20. V.V. Moshchalkov, X.G. Qiu, and V. Bruyndoncx, Phys. Rev. B **55**, 11 793 (1997); L.J. Barnes, and H.J. Fink, Phys. Lett. **20**, 583(1966); Phys. Rev. **149**, 186 (1966); H.J. Fink and A. G. Presson, *ibid.* **151**, 219 (1966).
21. A. Bezryadin, A. Buzdin, and B. Pannetier, Phys. Rev. B **51**, 3718 (1995).
22. J. Bardeen, Phys. Rev. Lett. **7**, 162 (1961).
23. V.M. Fomin, V.R. Misko, J.T. Devreese, and V.V. Moshchalkov, Phys. Rev. B **58**, 11 703 (1998).
24. V. Bruyndoncx, L. Van Look, M. Verschueren, and V.V. Moshchalkov, Phys. Rev. B **60**, 10 468 (1999).
25. L.F. Chibotaru, A. Ceulemans, V. Bruyndoncx, and V.V. Moshchalkov, Nature (London) **408**, 833 (2000); Phys. Rev. Lett. **86**, 1323 (2001).
26. V.R. Misko, V.M. Fomin, J.T. Devreese, and V.V. Moshchalkov, Phys. Rev. Lett. **90**, 147003 (2003).
27. L.R.E. Cabral, B.J. Baelus, and F.M. Peeters, Phys. Rev. B **70**, 144523 (2004).
28. R.C. Ashoori, Nature (London) **379**, 413 (1996).
29. V.M. Bedanov and F.M. Peeters, Phys. Rev. B **49**, 2667 (1994).

30. A.K. Geim, I. V. Grigorieva, S. V. Dubonos, J.G.S. Lok, J.C. Maan, A.E. Filippov, and F.M. Peeters, *Nature (London)* **390**, 256 (1997).
31. V.A. Schweigert and F. M. Peeters, *Phys. Rev. Lett.* **83**, 2409 (1999).
32. A. A. Abrikosov, *Fundamentals of the Theory of Metals* (North-Holland, Amsterdam, 1986).
33. A. I. Buzdin and J. P. Brison, *Phys. Lett. A* **196**, 267 (1994).
34. B.J. Baelus, F. M. Peeters, and V.A. Schweigert, *Phys. Rev. B* **63**, 144517 (2001).
35. A.K. Geim, S.V.Dubonos, J.J. Palacios, I.V. Grigorieva, M. Henini, and J.J. Schermer, *Phys. Rev. Lett.* **85**, 1528 (2000).
36. V.A. Schweigert and F.M. Peeters, *Physica C* **332**, 426 (2000).
37. B.J. Baelus, L.R.E. Cabral and F.M. Peeters, *Phys. Rev. B* **69**, 0604506 (2004).
38. L.J. Campbell and Robert M. Ziff, *Phys. Rev. B* **20**, 1886 (1979).
39. A.A.Abrikosov, *Sov. Phys. JETP* **5**, 1175 (1957).
40. A. Kanda, B.J. Baelus, F. M. Peeters, K. Kadowaki, and Y. Ootuka, *Phys. Rev. Lett.* **93**, 257002 (2004).
41. B.J. Baelus and F. M. Peeter, *Phys. Rev. B* **65**, 104515 (2002).
42. I.V. Grigorieva, W. Escoffier, J. Richardson, L. Y. Vinnikov, S. Dubonos, and V. Oboznov, *Phys. Rev. Lett.* **96**, 077005 (2006).
43. C. Reichhardt, C. J. Olson, and F. Nori, *Phys. Rev. B* **57**, 7939 (1998).
44. C. Reichhardt, C. J. Olson, and F. Nori, *Phys. Rev. Lett.* **78**, 2648 (1997),
C. Reichhardt, C. J. Olson, and F. Nori, *Phys. Rev. B* **58**, 6537 (1998).
45. V.R. Misko, S. Savelev, A.L. Rahnmanov, and R. Nori, *Phys. Rev. Lett.* **96**, 127004 (2006).
46. V. R. Misko, S. Savelev, and F. Nori, *Phys. Rev. Lett.* **95**, 177007 (2005),
Phys. Rev. B. **74**, 024522 (2006).
47. L.R.E. Cabral, B.J. Baelus, and F. M. Peeters, *Phys. Rev. B* **70**, 144523 (2004).
48. J. Bardeen and M.J. Stephen, *Phys. Rev.* **140**, A1197 (1965).
49. William H. Press, Brian P. Flannery, Saul A. Teukolsky, William T. Vetterling, *Numerical Recipes in FORTRAN 77* (Cambridge University Press, **1992**).